

EVIDENCE FOR WIDE-SPREAD ACTIVE GALACTIC NUCLEUS-DRIVEN OUTFLOWS IN THE MOST MASSIVE $z \sim 1-2$ STAR-FORMING GALAXIES*

R. GENZEL^{1,2,3}, N. M. FÖRSTER SCHREIBER¹, D. ROSARIO¹, P. LANG¹, D. LUTZ¹, E. WISNIOSKI¹, E. WUYTS¹, S. WUYTS¹, K. BANDARA¹, R. BENDER^{1,4}, S. BERTA¹, J. KURK¹, J. T. MENDEL¹, L. J. TACCONI¹, D. WILMAN^{1,4}, A. BEIFIORI^{1,4}, G. BRAMMER⁵, A. BURKERT^{1,4}, P. BUSCHKAMP¹, J. CHAN¹, C. M. CAROLLO⁶, R. DAVIES¹, F. EISENHAEUER¹, M. FABRICIUS¹, M. FOSSATI^{1,4}, M. KRIEK³, S. KULKARNI¹, S. J. LILLY⁶, C. MANCINI⁷, I. MOMCHEVA⁸, T. NAAB⁹, E. J. NELSON⁸, A. RENZINI⁷, R. SAGLIA^{1,4}, R. M. SHARPLES¹⁰, A. STERNBERG¹¹, S. TACHELLA⁶, AND P. VAN DOKKUM⁸

¹ Max-Planck-Institut für extraterrestrische Physik (MPE), Giessenbachstr.1, D-85748 Garching, Germany; forster@mpe.mpg.de, genzel@mpe.mpg.de

² Department of Physics, Le Conte Hall, University of California, Berkeley, CA 94720, USA

³ Department of Astronomy, Hearst Field Annex, University of California, Berkeley, CA 94720, USA

⁴ Universitäts-Sternwarte Ludwig-Maximilians-Universität (USM), Scheinerstr. 1, München D-81679, Germany

⁵ Space Telescope Science Institute, Baltimore, MD 21218, USA

⁶ Institute of Astronomy, Department of Physics, Eidgenössische Technische Hochschule, ETH Zürich, CH-8093, Switzerland

⁷ Osservatorio Astronomico di Padova, Vicolo dell'Osservatorio 5, Padova I-35122, Italy

⁸ Department of Astronomy, Yale University, P.O. Box 208101, New Haven, CT 06520-810, USA

⁹ Max-Planck Institute for Astrophysics, Karl Schwarzschildstrasse 1, D-85748 Garching, Germany

¹⁰ Department of Physics, Durham University, Science Laboratories, South Road Durham DH1 3LE, UK

¹¹ School of Physics and Astronomy, Tel Aviv University, Tel Aviv 69978, Israel

Received 2014 June 1; accepted 2014 August 29; published 2014 October 29

ABSTRACT

In this paper, we follow up on our previous detection of nuclear ionized outflows in the most massive ($\log(M_*/M_\odot) \geq 10.9$) $z \sim 1-3$ star-forming galaxies by increasing the sample size by a factor of six (to 44 galaxies above $\log(M_*/M_\odot) \geq 10.9$) from a combination of the SINS/zC-SINF, LUCI, GNIRS, and KMOS^{3D} spectroscopic surveys. We find a fairly sharp onset of the incidence of broad nuclear emission (FWHM in the $H\alpha$, [N II], and [S II] lines $\sim 450-5300 \text{ km s}^{-1}$), with large [N II]/ $H\alpha$ ratios, above $\log(M_*/M_\odot) \sim 10.9$, with about two-thirds of the galaxies in this mass range exhibiting this component. Broad nuclear components near and above the Schechter mass are similarly prevalent above and below the main sequence of star-forming galaxies, and at $z \sim 1$ and ~ 2 . The line ratios of the nuclear component are fit by excitation from active galactic nuclei (AGNs), or by a combination of shocks and photoionization. The incidence of the most massive galaxies with broad nuclear components is at least as large as that of AGNs identified by X-ray, optical, infrared, or radio indicators. The mass loading of the nuclear outflows is near unity. Our findings provide compelling evidence for powerful, high-duty cycle, AGN-driven outflows near the Schechter mass, and acting across the peak of cosmic galaxy formation.

Key words: galaxies: evolution – galaxies: high-redshift – galaxies: kinematics and dynamics – infrared: galaxies

Online-only material: color figures

1. INTRODUCTION

Throughout the last 10 billion years galaxies have been fairly inefficient in incorporating the cosmic baryons available to them into their stellar components. At a halo mass near $10^{12} M_\odot$ this baryon fraction is only about 20% (of the cosmic baryon abundance), and the efficiency drops to even lower values on either side of this mass (e.g., Madau et al. 1996; Baldry et al. 2008; Conroy & Wechsler 2009; Guo et al. 2010; Moster et al. 2010, 2013; Behroozi et al. 2013). Galactic winds driven by supernovae and massive stars have long been proposed to explain the low baryon content of halos much below $\log(M_h/M_\odot) \sim 12$ (e.g., Dekel & Silk 1986; Efstathiou 2000). The decreasing efficiency of galaxy formation above $\log(M_h/M_\odot) \sim 12$ may be caused by less efficient cooling and accretion of baryons in massive halos (Rees & Ostriker 1977; Dekel & Birnboim 2006). Alternatively or additionally efficient

outflows driven by accreting massive black holes may quench star formation at the high mass tail, at and above the Schechter stellar mass, $M_S \sim 10^{10.9} M_\odot$ (di Matteo et al. 2005; Croton et al. 2006; Bower et al. 2006; Hopkins et al. 2006; Cattaneo et al. 2006; Somerville et al. 2008; Fabian 2012).

In the local universe, such “AGN feedback” has been observed in the so-called “radio mode” in central cluster galaxies driving jets into the intra-cluster medium (Heckman & Best 2014; McNamara & Nulsen 2007; Fabian 2012), in ionized winds from Seyfert 2 AGNs (e.g., Cecil et al. 1990; Veilleux et al. 2005; Westmoquette et al. 2012; Rupke & Veilleux 2013; Harrison et al. 2014), and in powerful neutral and ionized gas outflows from buried AGNs in late-stage, gas-rich mergers (Fischer et al. 2010; Feruglio et al. 2010; Sturm et al. 2011; Rupke & Veilleux 2013; Veilleux et al. 2013; Arribas et al. 2014).

At high- z , AGN feedback has been observed in the so-called quasar mode in broad absorption line quasars (Arav et al. 2001, 2008, 2013; Korista et al. 2008), in type 2 AGNs (Alexander et al. 2010; Nesvadba et al. 2011; Cano Díaz et al. 2012; Harrison et al. 2012), and in radio galaxies (Nesvadba et al. 2008). However, luminous AGNs near the Eddington limit are rare. Luminous QSOs constitute $< 1\%$ of the star-forming population in the same mass range (e.g., Boyle et al. 2000). QSOs have short

* Based on observations obtained at the Very Large Telescope (VLT) of the European Southern Observatory (ESO), Paranal, Chile (ESO program IDs 073.B-9018, 074.A-9011, 075.A-0466, 076.A-0527, 078.A-0660, 079.A-0341, 080.A-0330, 080.A-0339, 080.A-0635, 081.A-0672, 082.A-0396, 183.A-0781, 087.A-0081, 088.A-0202, 088.A-0209, 091.A-0126, 092.A-0082, 092.A-0091, 093.A-0079). Also based on observations at the Large Binocular Telescope (LBT) on Mt. Graham in Arizona.

lifetimes relative to the Hubble time ($t_{\text{QSO}} \sim 10^7\text{--}10^8 \text{ yr} \ll t_{\text{H}}$; Martini 2004) and thus low duty cycles compared to galactic star formation processes ($t_{\text{SF}} \sim 10^9 \text{ yr}$; Hickox et al. 2014). It is thus not clear whether the radiatively efficient “quasar mode” can have much effect in regulating galaxy growth and star formation shutdown, as postulated in the theoretical work cited above (Heckman 2010; Fabian 2012).

From deep SINFONI adaptive optics assisted (AO) observations at the ESOVLT, Förster Schreiber et al. (2014a, henceforth FS14a) have recently reported the discovery of broad ionized gas emission associated with the nuclear regions of very massive ($\log(M_*/M_\odot) > 10.9$) $z \sim 2$ main-sequence star-forming galaxies (SFGs) observed as part of the SINS/zC-SINF surveys (Förster Schreiber et al. 2009; N. M. Förster Schreiber et al. 2014b, in preparation; Mancini et al. 2011). For the seven galaxies with the best data quality enabling a quantitative analysis, all exhibit

1. a very broad, centrally concentrated emission component with FWHM $> 1000 \text{ km s}^{-1}$ in the $\text{H}\alpha$ and $[\text{N II}]$ (and probably the $[\text{S II}] \lambda\lambda 6716/6731$) lines, which coincides with the location of a massive stellar bulge revealed by *Hubble Space Telescope* (HST) near-IR imaging. In several galaxies this broad component is resolved by the AO observations, indicating an intrinsic FWHM diameter of 2–3 kpc, and
2. a (circum-)nuclear ratio of the narrow emission component $[\text{N II}]/\text{H}\alpha$ line fluxes of 0.5–0.8, at or above the limit of normal stellar photoionized H II regions, and akin to type 2 AGNs.

The fact that the broad emission component is present in the forbidden $[\text{N II}]$ lines as well as its kiloparsec-size extent excludes that the broad emission comes from a virialized, parsec-scale AGN broad-line region (BLR) in these cases. If so, the $> 1000 \text{ km s}^{-1}$ velocity range on kiloparsec scales implies that the broad component cannot be gravitationally bound and must represent a circum-nuclear outflow in the kiloparsec-scale “narrow-line region” (Netzer 2013). The substantial flux ratio of $F(\text{H}\alpha_{\text{broad}})/F(\text{H}\alpha_{\text{narrow}}) \sim 0.3\text{--}1$ found in these galaxies then suggests the mass loading of these nuclear outflows is substantial ($dM_{\text{out}}/dt/\text{SFR} \sim 1$; FS14a).

Based on X-ray and mid-infrared indicators, AGN incidence at $z > 1$ increases from a few percent at $\log(M_*/M_\odot) \sim 10\text{--}10.5$ up to $\sim 15\%\text{--}30\%$ at $\log(M_*/M_\odot) > 11$ (e.g., Reddy et al. 2005; Papovich et al. 2006; Daddi et al. 2007; Brusa et al. 2009, 2014; Hainline et al. 2012; Bongiorno et al. 2012). *Herschel* studies have revealed that the AGN host population is mainly drawn from normal main-sequence SFGs (e.g., Mullaney et al. 2012; Rosario et al. 2012, 2013b). As such, the identification of AGN-driven outflows in high-mass SFGs may not come as a surprise in a qualitative sense. The tantalizing new and exciting element in FS14a is the possible identification of a nuclear ionized outflow component in a large fraction of such massive, star-forming hosts that may be driven by a central AGN. However, the small size of the FS14a sample prevents any firm conclusion on the incidence and properties of the detected nuclear outflows, although an inspection of various other $z \sim 2$ small galaxy samples in the literature (Erb et al. 2006; Kriek et al. 2007; Swinbank et al. 2012, as discussed in FS14a) are consistent with a fairly large incidence.

In this paper, we have followed up on these results and present a much larger sample compared to the SINS/zC-SINF sample of FS14a, which includes in particular six times more galaxies

at $\log(M_*/M_\odot) \geq 10.9$. We combine the samples from the SINS and zC-SINF surveys (Förster Schreiber et al. 2009; N. M. Förster Schreiber et al. 2014b, in preparation; Mancini et al. 2011) with SINFONI (Eisenhauer et al. 2003; Bonnet et al. 2004), together with first epoch data from our KMOS^{3D} survey of mass-selected SFGs at $0.7 < z < 2.7$ (Wisnioski et al. 2014) obtained with the new KMOS near-IR multi-IFU instrument on the VLT (Sharples et al. 2012, 2013), massive $z \sim 1.5\text{--}2.5$ SFGs from our ongoing spectroscopic survey with the LUCI near-IR multi-object spectrograph at the Large Binocular Telescope (LBT; Wuyts et al. 2014a), and massive $z \sim 2\text{--}2.5$ SFGs from the *K*-band selected near-IR spectroscopic sample of Kriek et al. (2007) observed with SINFONI and with GNIRS at Gemini South. With significantly improved statistics, a wider coverage in specific star formation rate (sSFR) and in redshift, the sample studied here allows us to substantially strengthen our previous findings about the onset and properties of nuclear AGN-driven outflows above the Schechter mass, and to explore trends with redshift and with location of galaxies above or below the main sequence of SFGs.

Throughout, we adopt a Chabrier (2003) stellar initial mass function and a Λ CDM cosmology with $H_0 = 70 \text{ km s}^{-1}$ and $\Omega_m = 0.3$.

2. OBSERVATIONS

2.1. Data Sets

For the analysis in this paper, we included a total of 110 SFGs at $z \sim 1\text{--}3$ with near-IR integral field or slit spectroscopy covering the $\text{H}\alpha + [\text{N II}]$ line emission from surveys carried out with SINFONI, KMOS, LUCI, and GNIRS. The targets for these surveys were originally drawn from rest-frame optical, UV, and near-IR selected samples in broadband imaging surveys with optical spectroscopic redshifts, and from stellar mass-selected samples with near-IR or optical spectroscopic redshifts. Global stellar properties for all the galaxies were derived following similar procedures as outlined by Wuyts et al. (2011a). In brief, stellar masses were obtained from fitting the rest-UV to near-IR spectral energy distributions (SEDs) with Bruzual & Charlot (2003) population synthesis models, the Calzetti et al. (2000) reddening law, a solar metallicity, and a range of star formation histories (including constant SFR and exponentially declining SFRs with varying e -folding timescales). SFRs were obtained from the same SED fits or, for objects observed and detected in at least one of the mid- to far-IR (24–160 μm) bands with the *Spitzer*/MIPS and *Herschel*/PACS instruments, from rest-UV+IR luminosities through the *Herschel*-calibrated ladder of SFR indicators of Wuyts et al. (2011a). Details of the derivations are given in the references below; we note that the methods and model assumptions were similar for the different subsamples (and we corrected the M_* and SFR estimates to our adopted Chabrier IMF when necessary), ensuring consistency for the present study.

Of the full near-IR spectroscopic samples considered, we retained the 110 objects that have the high-quality and signal-to-noise (S/N) ratio (line detections with $\text{S/N} > 10$) spectra required for our analysis and that do not have strong contamination by atmospheric OH sky emission around the $\text{H}\alpha + [\text{N II}]$ complex. The galaxies have redshifts between $z = 0.8$ and 2.6 and stellar masses in the range $\log(M_*/M_\odot) = 9.4\text{--}11.7$. Most are spatially resolved in their $\text{H}\alpha + [\text{N II}]$ line emission. The sample consists of the following subsets.

1. 33 SFGs with $\log(M_*/M_\odot) = 9.4\text{--}11.5$ from the $z \sim 1.5\text{--}2.5$ SINS/zC-SINF survey (Förster Schreiber et al. 2009; Mancini et al. 2011); all but four of these galaxies were observed in AO mode resulting in a typical $0''.2\text{--}0''.3$ FWHM resolution. The four SFGs observed only in seeing limited mode ($0''.5\text{--}0''.6$ FWHM resolution) were either well resolved at that resolution (three cases), or strongly dominated by the nuclear region (one case). In two large and well-resolved SFGs we combined AO and seeing limited data sets to further improve the S/N of the spectra.
2. 56 galaxies with $\log(M_*/M_\odot) = 10.0\text{--}11.7$ at $z = 0.8\text{--}1.1$ and $z = 2\text{--}2.6$ observed in natural seeing with KMOS during commissioning and the first year of our KMOS^{3D} survey (Wisnioski et al. 2014) carried out as part of guaranteed time observations (GTO). These galaxies form a subset of the total of 210 targets observed (and 174 detected in H α) so far¹², emphasizing the massive part of the sample. They include (1) all targets at $\log(M_*/M_\odot) > 10.6$ with emission line detections and (2) the subset of targets at $\log(M_*/M_\odot) < 10.6$ that are sufficiently well resolved and exhibit evidence of rotation in their kinematic maps.
3. 10 SFGs at $z = 1.5\text{--}2.5$ with $\log(M_*/M_\odot) > 10.6$ from our LUCI multi-object slit spectroscopic survey in natural seeing at the LBT (Wuyts et al. 2014a). This LUCI sample includes the large $\log(M_*/M_\odot) = 11.0$ SFG EGS-13011166 observed in CO molecular line emission as part of the “PHIBSS1” survey of Tacconi et al. (2013), and for which we obtained high quality spatially resolved H α + [N II] emission from slit mapping with LUCI ($\sim 0''.6$ FWHM resolution; Genzel et al. 2013).
4. 1 $\log(M_*/M_\odot) = 11.5$ lensed main-sequence SFG (J0901+1814; Diehl et al. 2009; Saintonge et al. 2013), for which we obtained deep, seeing limited and AO SINFONI data. The no-AO and AO data were combined together to increase the S/N and, accounting for the lensing magnification, the effective source plane resolution is $\sim 0''.1$ (E. Wuyts et al. 2014b, in preparation).
5. 10 $\log(M_*/M_\odot) \geq 11$ emission line galaxies from the K-band selected $z \sim 2\text{--}2.5$ near-IR spectroscopic sample of Kriek et al. (2007) observed with GNIRS and SINFONI in seeing-limited mode. The SINFONI data alone have too low S/N for our analysis, so we used the combined GNIRS+SINFONI spectra as published by Kriek et al. with the following exception. For one object (SDSS 1030–2026), lying a factor of ~ 30 in specific SFR below the $z = 2.5$ main sequence, we recently obtained SINFONI AO-assisted observations, which clearly confirm the presence of a spatially compact and spectrally broad emission line component.

Ranked by ascending stellar mass into four bins, $\log(M_*/M_\odot) = [9.4\text{--}10.3]$, $[10.3\text{--}10.6]$, $[10.6\text{--}10.9]$, and $[10.9\text{--}11.7]$, our sample breaks up into 17, 19, 30, and 44 SFGs, respectively. In the two most critical highest mass bins, there are each six times more galaxies as in the set available to FS14a.

The distribution of the final sample in stellar mass versus specific SFR is shown in Figure 1, along with that of the underlying population of mass-selected galaxies from the 3D-HST Treasury survey (Brammer et al. 2012; Skelton et al.

2014) in the same $z = 0.8\text{--}2.6$ range. To account for the global evolution of star formation properties of galaxies with cosmic time, the specific SFR of every object is computed and plotted relative to the value of the main sequence at its respective redshift and stellar mass, denoted sSFR/sSFR(ms), adopting the parameterization of Whitaker et al. (2012)¹³. Of the 110 SFGs of our sample, 92 lie within ± 0.6 dex of the main sequence; they span two orders of magnitude in stellar mass, and cover approximately homogeneously the mass and specific SFR range of the main sequence above $\log(M_*/M_\odot) \sim 10.3$. Three SFGs are outliers above the main sequence. The remaining 14 galaxies, all from the KMOS^{3D}, LUCI, and Kriek et al. (2007) samples, extend our coverage to significantly below the main sequence, with 6 of them having very low specific SFRs (< 0.06 of the main sequence).

A kinematic classification is possible for the 93 of the 110 SFGs that have IFU data (this includes the Keck/OSIRIS data published by Law et al. (2012) for one of our LUCI targets, Q2343-BX442). In terms of kinematics, 73 of these sources have a ratio of rotation/orbital velocity to intrinsic velocity dispersion $v_{\text{rot}}/\sigma_0 > 1$ and are plausibly rotating disks (see Newman et al. 2013; Wisnioski et al. 2014). Although we emphasized objects with evidence for rotation in choosing the lower-mass KMOS^{3D} objects for this study, the high disk fraction is not surprising and consistent with the growing evidence that a majority of massive $z \sim 1\text{--}2.5$ SFGs are disks based on kinematic and morphological properties (see also, e.g., Shapiro et al. 2008; Genzel et al. 2008, 2014a; Förster Schreiber et al. 2009; Épinat et al. 2009, 2012; Jones et al. 2010; Wuyts et al. 2011b; Lang et al. 2014). Three sources are identified as candidate minor mergers, and four are candidate major mergers. Seven of the lower mass galaxies ($\log(M_*/M_\odot) < 10.4$) show no or little evidence for rotational support and are classified as “dispersion dominated.” Three compact galaxies in the highest mass bin exhibit little evidence for narrow line emission as expected from star formation activity and are completely dominated by very broad line emission, probably due to a type I AGN broad line region. These three objects will hereafter be referred to as “candidate BLR sources.” Our preferential inclusion of rotating systems among the lower mass KMOS^{3D} targets may tend to emphasize larger galaxies that are more easily resolved in seeing-limited KMOS data, although SINFONI targets with higher resolution AO data dominate at the low- M_* end of the present sample; we return to this point below. These kinematic identifications are listed in Column 3 of Table 1, which also summarizes the salient parameters of our sample.

We verified that the requirements imposed when selecting the objects for our study do not introduce significant biases that would affect the results of our analysis, in particular the need for an H α detection, the emphasis on high-quality and S/N data sets, and the preferential inclusion of better resolved objects toward lower masses from KMOS^{3D}. To this aim, we considered the sSFR and size distributions in the M_* bins defined above of all

¹² KMOS^{3D} is a multi-year survey; the current sample includes a fraction of targets for which only part of the planned integration time has been obtained and which will be further observed in subsequent semesters.

¹³ The exact parameterization of the main sequence of SFGs varies among different studies, which is attributed to the impact of different sample selection, survey completeness, methodology applied to derive the stellar masses and SFRs, among other factors. The Whitaker et al. (2012) fits provide a good representation of the locus of SFGs in our comparison 3D-HST sample above $\log(M_*/M_\odot) \sim 10.3$, encompassing our three highest mass bins comprising 85% of our sample. At lower masses, a difference becomes apparent (see Figure 1); an alternative fit to main-sequence SFGs from 3D-HST is beyond the scope of this paper, so we keep the Whitaker et al. parameterization bearing in mind that the quantitative offset from the main sequence of our $\log(M_*/M_\odot) < 10.3$ galaxies could be more uncertain.

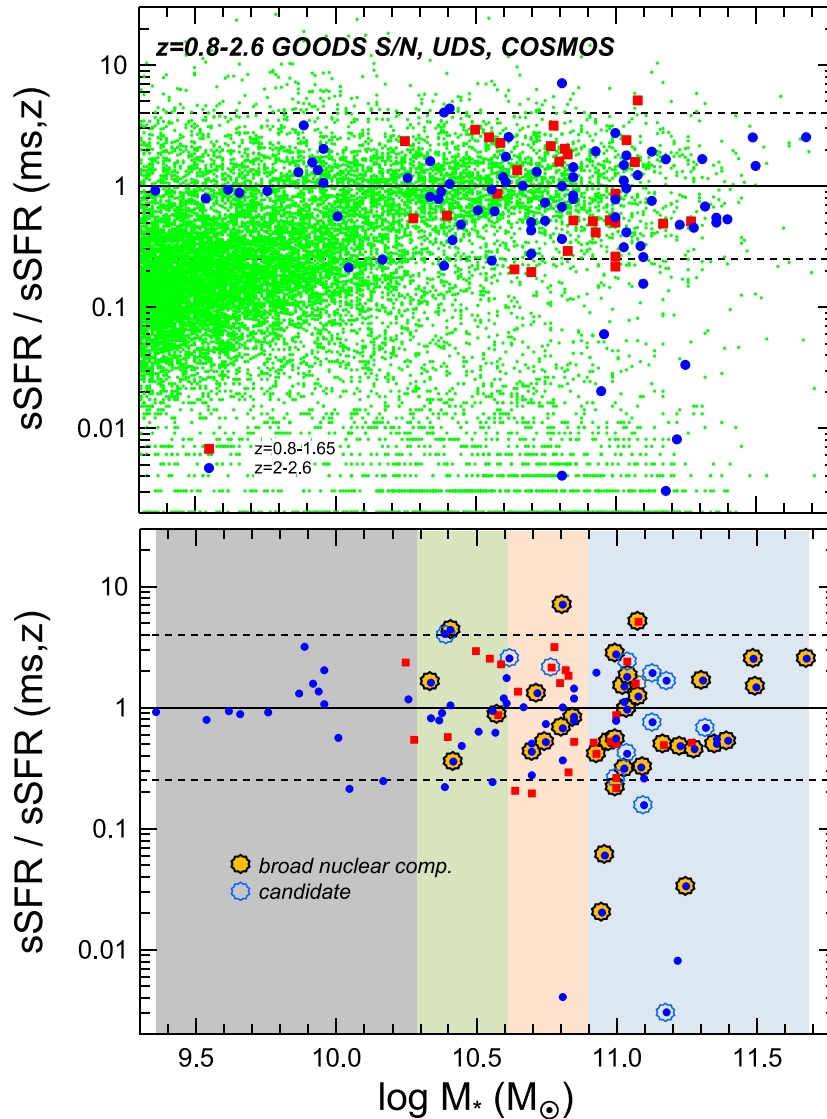


Figure 1. Top panel: location of our final $z = 0.8\text{--}2.6$ SFG sample of 110 galaxies in the stellar-mass-specific star formation rate (sSFR) plane. We have divided the sSFR of each galaxy by the value of the main sequence line (as determined from the Whitaker et al. (2012) fitting function valid for $>10^{10} M_{\odot}$) for a fair comparison of galaxies at different redshifts. Red squares denote $z \sim 0.8\text{--}1.6$ and blue circles $z \sim 2\text{--}2.6$ SFGs from the SINS/zC-SINF surveys (Förster Schreiber et al. 2009, 2014b, in preparation; Mancini et al. 2011), the LUCI survey (Wuyts et al. 2014a), the first-year KMOS^{3D} survey results (Wisnioski et al. 2014), and the GNIRS+SINFONI survey of massive galaxies by Kriek et al. (2007). The small green dots represent the samples drawn from 3D-*HST* survey catalogs of $z = 0.8\text{--}2.6$ galaxies in the CANDELS, GOODS N/S, COSMOS, and UDS fields (e.g., Wuyts et al. 2011a, 2011b; Brammer et al. 2012; Skelton et al. 2014). Bottom: the shaded vertical regions denote the four mass bins discussed throughout the text (gray: $\log M_{*} = 9.4\text{--}10.3$, green: $10.3\text{--}10.6$, pink: $10.6\text{--}10.9$, blue: $10.9\text{--}11.7$). Large orange-filled black circles denote those galaxies in which the individual nuclear spectra exhibit a significant broad component. Open blue circles denote less certain candidates with possible broad components.

(A color version of this figure is available in the online journal.)

objects from the parent KMOS^{3D}, SINS/zC-SINF, LUCI, and GNIRS+SINFONI near-IR spectroscopic samples, and of the underlying population of SFGs in the same stellar mass and redshift ranges (taken from the 3D-*HST* survey, and defined as having an inverse sSFR greater than three times the Hubble time at their redshift). For the sizes, we used the major axis effective radius measured from *HST* *H*-band imaging, available for $>90\%$ of the objects in the near-IR spectroscopic samples and the 3D-*HST* survey (Table 1, and also van Dokkum et al. 2008; Kriek et al. 2009; Förster Schreiber et al. 2011; Lang et al. 2014; van der Wel et al. 2014; Tacchella et al. 2014).

Altogether, the fractions of $H\alpha$ -detected objects among the full parent near-IR spectroscopic samples are $\sim 80\%$ – 90% in the three lowest M_{*} bins. The $H\alpha$ detection fraction drops to $\sim 65\%$

in the highest M_{*} bin, which is largely driven by the fact that we also included objects well below the main sequence (i.e., at very low sSFRs) in our observations. There is a trend of somewhat lower detection fractions for objects below the main sequence or with sizes smaller than the median over all SFGs (from $\sim 90\%$ to $\sim 60\%$ between low- and high- M_{*} bins, compared to $\sim 90\%$ to 75% for objects above the main sequence or with sizes larger than the median for SFGs), again driven by targets with low sSFR/sSFR(ms) < 0.1 that also tend to be more compact (e.g., van der Wel et al. 2014). These detection fractions and trends are essentially the same when considering only the KMOS^{3D} targets observed so far and with their current integration times.

In terms of range and median values, the sSFR/sSFR(ms) and size distributions of the underlying SFG population are overall

Table 1
SFG Sample

Source	Survey	Kinematics ^a	Mode ^b	T_{int}^c (h)	S/N center	Broad ^d	z	\log (M_*/M_{\odot})	sSFR/sSFR (ms) ^e	[N II]/H α Center	$R_{1/2}$ (kpc)	AGN	\log ($L(\text{AGN})/\text{erg s}^{-1}$) ^f	$L(\text{SFR})/$ $L(\text{AGN})$ ^g
SSA22a-MD41	SINS/zC-SINF	disk	Ss	7	16	...	2.17	9.89	3.131	0.12	5.1
ZC-405501	SINS/zC-SINF	disk	AO	5.7	9	...	2.15	9.92	1.552	0.08	7.7
ZC-413507	SINS/zC-SINF	disk	AO	5.8	8	...	2.48	9.94	1.335	0.10	3.6	cand
ZC-405226	SINS/zC-SINF	disk	AO	12.3	10	...	2.29	9.96	2.003	0.33	4.4
ZC-413597	SINS/zC-SINF	disp	AO	5.8	9	...	2.44	9.87	1.287	0.11	2.5
ZC-415876	SINS/zC-SINF	disk	AO	5.8	11	...	2.44	9.96	1.050	0.12	1.9
GMASS-2438	SINS/zC-SINF	disk	ss	3.7	6	...	1.62	10.25	2.327	0.39	8.0
Q2346-BX482	SINS/zC-SINF	disk	AO	12.3	6	...	2.26	10.26	1.151	0.26	5.5
Q1623-BX502	SINS/zC-SINF	disk	AO	6.3	30	...	2.16	9.36	0.905	0.05	1.3
ZC-411737	SINS/zC-SINF	disk	AO	4.2	8	...	2.44	9.54	0.781	0.06	3.1	cand
ZC-410123	SINS/zC-SINF	disk-disp	AO	2	7	...	2.20	9.62	0.919	0.10	4.8
ZC-410041	SINS/zC-SINF	disk	AO	6	7	...	2.45	9.66	0.868	0.05	5.0
ZC-401925	SINS/zC-SINF	disp	AO	3.5	12	...	2.14	9.76	0.898	0.08	2.5
Q1623-BX455	SINS/zC-SINF	disk	AO	3.5	11	...	2.41	10.01	0.553	0.20	2.0
U3-10523	KMOS ^{3D}	disp	s	7.1	25	...	2.16	10.05	0.210	0.18	1.2
U3-15027	KMOS ^{3D}	disp	s	7.1	10	...	2.29	10.17	0.244	0.29	2.7
GMASS-2540	SINS/zC-SINF	disk	AO	10	11	...	1.61	10.28	0.535	0.29	11.2
ZC-412369	SINS/zC-SINF	disp	AO	4	28	1	2.03	10.34	1.584	0.22	3.8
SA12-6339	SINS/zC-SINF	disp	AO	7.8	40	2	2.30	10.41	4.307	0.18	1.6
ZC-407302	SINS/zC-SINF	disk, merger?	AO	19	30	0.5	2.18	10.39	4.003	0.24	4.6
U3-6856	KMOS ^{3D}	disk	ss	7	11	...	2.30	10.41	1.027	0.21	1.9
COS3-21583	KMOS ^{3D}	disk	ss	1.7	20	...	0.89	10.50	2.887	0.25	4.4
COS3-1705	KMOS ^{3D}	disk	ss	3.7	50	...	0.83	10.55	2.502	0.35	7.5
GS3-24369	KMOS ^{3D}	disk	s	8.2	27	...	0.89	10.59	2.245	0.43	1.9
GMASS-2363	SINS/zC-SINF	disk	AO	13.7	10	...	2.45	10.34	0.803	0.14	2.4
COS4-5094	KMOS ^{3D}	disk	ss	11.3	13	...	2.17	10.38	0.887	0.27	5.1
U3-10584	KMOS ^{3D}	disk	ss	7	18	...	2.24	10.37	0.771	0.18	4.7	cand
GS3-26790	KMOS ^{3D}	disk	ss	8.9	17	...	2.23	10.39	0.217	0.08	4.4
U3-3856	KMOS ^{3D}	disk	ss	4.5	10	...	0.80	10.40	0.565	0.38	4.7
U3-27143	KMOS ^{3D}	disk	ss	7	25	2	2.26	10.42	0.353	0.22	1.6
GS3-26192	KMOS ^{3D}	disk-disp	s	8.9	25	...	2.32	10.45	0.475	0.10	2.6
COS4-15813	KMOS ^{3D}	disk	ss	8.2	20	...	2.36	10.57	0.612	0.10	2.5
COS4-4453	KMOS ^{3D}	disp	s	11.3	6	...	2.44	10.56	0.239	0.34	3.1
K20-ID8	SINS/zC-SINF	disk	ss	3.7	23	...	2.22	10.51	0.622	0.29	6.0
GS3-22466	KMOS ^{3D}	disk	ss	8.9	8	...	2.23	10.56	0.923	0.28	3.9
GS3-27242	KMOS ^{3D}	disk	s	8.2	2	1	1.03	10.58	0.856	0.51	2.6
Q2343-BX389	SINS/zC-SINF	disk	AO	5	15	...	2.17	10.61	1.067	0.20	6.8
ZC-406690	SINS/zC-SINF	disk	AO	10	6	0.5	2.20	10.62	2.508	0.27	5.5
ZC-403741	SINS/zC-SINF	disk	AO	4	22	...	1.45	10.65	1.339	0.53	2.5
K20-ID7	SINS/zC-SINF	disk	AO	7.2	2.22	10.60	1.174	0.22	8.4
COS3-23443	KMOS ^{3D}	disk	ss	1.7	2	0.5	0.89	10.77	2.114	0.80	5.9
COS3-16954	KMOS ^{3D}	disk	ss	9.2	16	...	1.03	10.78	3.123	0.76	7.1
COS3-25038	KMOS ^{3D}	disk	ss	1.7	15	...	0.85	10.80	1.573	0.37	25.0
GS3-18419	KMOS ^{3D}	disk	ss	8.9	14	2	2.31	10.81	6.975	0.70	2.8	det	<45.3	18
COS4-4519	KMOS ^{3D}	disk	ss	11.3	20	...	2.23	10.61	1.729	0.30	2.4	cand
COS3-18434	KMOS ^{3D}	disk	ss	3.7	20	...	0.91	10.82	2.014	0.46	4.3
COS4-19680	KMOS ^{3D}	disk	ss	8.2	2.17	10.85	1.415	0.55	2.4
COS4-10347	KMOS ^{3D}	disk	ss	19.8	11	...	2.06	10.85	1.171	0.39	4.0	cand
COS3-4796	KMOS ^{3D}	disk	ss	3.7	5	...	1.03	10.83	1.805	0.42	6.5
ECDFS-10525	GNIRS+SINFONI	...	s	3	2	1	2.02	10.72	1.296	0.50	...	det	<45.6	1.3
U3-8493	KMOS ^{3D}	disk	ss	4.5	12	...	0.79	10.64	0.203	0.57	2.4
GS3-24364	KMOS ^{3D}	disk-disp	ss	8.9	25	...	2.33	10.70	0.497	0.17	5.3
COS4-13701	KMOS ^{3D}	disk	ss	8.2	25	...	2.17	10.67	0.991	0.23	4.0
COS3-11468	KMOS ^{3D}	...	s	4.2	weak	...	0.89	10.83	0.288	no	3.7
Q1623-BX599	SINS/zC-SINF	disk, merger?	AO	2	25	1	2.33	10.75	0.511	0.17	3.1
Q1623-BX663	SINS/zC-SINF	disk	AO-s	8.8	15	2	2.43	10.81	0.664	0.43	6.5	det	<46.0	0.35
U3-25105	KMOS ^{3D}	disk	ss	7	12	1	2.29	10.85	0.826	0.50	6.0	cand
U3-13321	KMOS ^{3D}	disk	ss	4	2	...	0.91	10.85	0.515	0.82	3.6
GOODSN-19394	LUCI	...	s	4	1.45	10.7	0.193	0.19	21.0
GOODSN-31720	LUCI	...	s	4	2.48	10.7	0.272	0.23	...	cand
GOODSN-03493	LUCI	...	s	4	2.46	10.8	0.364	0.40	...	cand
GOODSN-07923	LUCI	BLR	s	4	...	2	2.24	10.7	0.425	broad	...	det	45.6	0.5
1030-807	GNIRS+SINFONI	...	s	3	2.37	10.81	0.004	0.33	3.3
ECDFS-5754	GNIRS+SINFONI	...	s	3	2.04	10.81	0.989	0.20	5.5
COS4-18859	KMOS ^{3D}	...	s	8.2	2.61	10.75	0.720	no	0.8
COS4-16342	KMOS ^{3D}	disk	s	8.2	8	...	2.47	10.85	0.772	0.27	5.1	cand
COS4-4717	KMOS ^{3D}	disk	s	11.3	9	...	2.44	10.93	1.916	0.36	4.1	cand
ZC-400528	SINS/zC-SINF	disk+merger	AO	4	20	2	2.39	11.04	1.768	0.75	2.0

Table 1
(Continued)

Source	Survey	Kinematics ^a	Mode ^b	T_{int}^c (h)	S/N center	Broad ^d	z	$\log(M_*/M_\odot)$	sSFR/sSFR (ms) ^e	[N II]/H α Center	$R_{1/2}$ (kpc)	AGN	$\log(L(\text{AGN})/\text{erg s}^{-1})^f$	$L(\text{SFR})/L(\text{AGN})^g$
D3a-6397	SINS/zC-SINF	disk	AO	8.5	18	2	1.50	11.08	5.052	0.77	6.0
ZC-400569 central disk	SINS/zC-SINF	disk+merger	AO	22	18	1	2.24	11.08	1.213	0.73	6.4
GS3-31118	KMOS ^{3D}	disk	ss	4.4	8	0.5	2.45	11.13	1.898	1.49	1.1	cand
U3-16262	KMOS ^{3D}	disk	ss	5.8	11	0.5	2.30	11.18	1.642	0.63	2.5	cand
GS3-19791 (K20-ID5)	KMOS ^{3D}	disk	ss	4.4	30	2	2.22	11.31	1.649	0.80	3.6	det	44.6	29
D3a-6004	SINS/zC-SINF	disk	AO	4.7	9	2	2.39	11.50	1.446	1.09	5.0
J0901+1814	SINFONI	disk	AO	9	10	2	2.26	11.49	2.489	0.87	2.0	det
EGS13011166	LUCI	disk	ss	12	8	0.5	1.53	11.04	2.367	0.56	6.0	det
D3a-7144	SINS/zC-SINF	disk	s	2	9	0.5	1.65	11.07	1.565	0.87	4.6	det
COS4-14596	KMOS ^{3D}	BLR	ss	8.2	...	2	2.44	11.68	2.503	broad	0.2	det	45.8	5
COS4-13174	KMOS ^{3D}	disk	ss	19.7	15	1	2.10	11.03	1.469	0.48	6.4	cand
COS4-10056	KMOS ^{3D}	disk	s	19.7	5	...	2.56	11.03	1.096	0.50	4.5
COS4-21492	KMOS ^{3D}	BLR	s	8.1	...	2	2.47	11.00	2.707	broad	0.4	det	46.1	1.4
COS4-6963	KMOS ^{3D}	merger?	s	11.3	8	2	2.30	10.96	0.059	0.20	2.2
GS3-21045	KMOS ^{3D}	disk	ss	8.2	12	...	0.96	10.92	0.506	0.85	9.2
GS3-22005	KMOS ^{3D}	disk	ss	8.2	10	1	0.95	10.93	0.410	0.53	32.0
U3-12280	KMOS ^{3D}	disk+merger	ss	8.9	7	2	1.03	10.98	0.516	0.83	4.1
Q2343-BX610	SINS/zC-SINF	disk	AO	8.3	22	2	2.21	11.00	0.548	0.58	8.0
U3-15226	KMOS ^{3D}	disk	ss	8.9	10	...	0.92	11.00	0.856	0.85	5.8
D3a-15504	SINS/zC-SINF	disk	AO	23	30	2	2.38	11.04	0.949	0.48	6.7	det
GS3-28464	KMOS ^{3D}	disk	ss	17	3	0.5	2.30	11.04	0.409	0.54	1.9	det	44.4	10
GS3-25445	KMOS ^{3D}	disk	ss	4.4	12	0.5	2.43	11.13	0.744	0.55	0.7
COS3-644	KMOS ^{3D}	disk	ss	3.7	10	1	0.88	11.17	0.484	0.99	5.0
COS3-8390	KMOS ^{3D}	disk	ss	3.7	2	...	0.98	11.27	0.505	1.00	3.8
U3-23710	KMOS ^{3D}	disk	ss	7.1	10	2	2.53	11.03	0.309	0.59	4.7
GS3-28008	KMOS ^{3D}	nucleus only	ss	17	4	2	2.29	11.36	0.493	0.87	3.3	det	45.9	0.5
GS3-7562	KMOS ^{3D}	disk	ss	7.5	2	0.5	2.04	11.32	0.670	0.20	6.5
GOODSN-29999	LUCI	...	s	4	1.53	11	0.493	0.40
GOODSN-22747	LUCI	...	s	4	5	2	1.45	11	0.214	1.30	...	det	45.9	0.08
GOODSN-22412	LUCI	...	s	4	5.3	0.5	1.52	11	0.259	0.30
Q2343-BX442	LUCI	disk	s	4	2.18	11.1	0.256	OH
GOODSN-17020	LUCI	...	s	4	...	0.5	2.33	11.1	0.154	1.20	...	det	44.6	2.6
1030-1531	GNIRS+SINFONI	...	s	3	2.61	11	0.765	0.35	3.9
1030-2026	GNIRS+SINFONI	...	s	3.1	4	2	2.51	11.25	0.033	0.64	1.5	det
1030-2329	GNIRS+SINFONI	...	s	3	3	1	2.24	10.95	0.020	0.71	1.3
1030-2728	GNIRS+SINFONI	...	s	2	1	0.5	2.50	11.18	0.003	0.63	1.0
ECDFS-3662	GNIRS+SINFONI	...	s	3	2	1	2.35	11.09	0.316	0.56	1.7
ECDFS-3694	GNIRS+SINFONI	...	s	4	2.12	11.36	0.541	0.45	8.6
ECDFS-3896	GNIRS+SINFONI	...	s	2	1.5	2	2.31	11.23	0.473	1.09	1.7
COS4-3206	KMOS ^{3D}	disk	ss	11.5	10	1	2.10	11.40	0.525	0.60	6.2	det	<45.7	0.84
COS4-11363	KMOS ^{3D}	merger?	s	19.7	33	2	2.10	11.28	0.447	0.60	2.2	det	46.3	0.2
COS4-12995	KMOS ^{3D}	disk	s	19.7	1.2	...	2.44	11.22	0.008	1.50	1.4	cand

Notes.

^a Kinematic classification of galaxy from H α data; “disk” stands for rotation, “disp” for dispersion dominated kinematics, “merger” for perturbed motions in a major merger system, and “BLR” for a compact AGN broad line region component.

^b Observing mode for the data used in this work. “AO” indicates adaptive-optics-assisted observations with FWHM resolution of 0'2–0'3; “s” and “ss” indicate seeing-limited observations with FWHM resolution of 0'5–0'7 (“s” denotes objects for which the kinematics are well resolved).

^c Total on-source integration time of the observations.

^d Identification of a broad nuclear emission component: “2” for a strong nuclear broad component, “1” for a clear nuclear broad component, and “0.5” for a candidate nuclear broad component.

^e Specific SFR normalized to that of the main sequence of SFGs at the redshift and stellar mass of each object using the parameterization of Whitaker et al. (2012), applicable for $\log(M_*/M_\odot) > 10$.

^f The bolometric AGN luminosity is estimated either from the absorption corrected X-ray luminosity (as in Rosario et al. 2012), or from the rest-frame 8 μm luminosity of power-law mid-IR SEDs extrapolated to the total blue bump luminosity with AGN SEDs (Richards et al. 2006), or an average. If only a mid-IR estimate is available, we consider this luminosity an upper limit to the AGN luminosity.

^g Ratio of the AGN to galaxy integrated star formation rate luminosity (assuming $L(\text{SFR}) = 1 \times 10^{10} \times \text{SFR}$).

well covered by the parent near-IR spectroscopic samples as well as by the H α -detected subsets and the objects included in the present study. The most significant differences are as follows. In the lowest M_* bin, the parent near-IR spectroscopic samples preferentially probe the part of the SFG population with higher sSFR/sSFR(ms) and larger sizes, by factors of around 3 and 1.8 in the median (due in part to their M_* distribution weighted toward the more massive objects compared to the bulk

of SFGs in that M_* interval). The same trend applies to the H α -detected subset and to the objects analyzed in this paper. At $\log(M_*/M_\odot) < 10.3$, our sample is largely dominated by SINS/zC-SINF galaxies at $z \sim 1.5$ –2.5 with AO-assisted SINFONI observations (Table 1), for which the typically three to four times higher resolution compared to seeing-limited data helps to better resolve smaller objects (see also Newman et al. 2013). Toward higher masses, the SFG population is well covered and, in

addition, the objects from the KMOS^{3D} and GNIRS+SINFONI parent samples extend to lower sSFR/sSFR(ms) and smaller sizes than the bulk of SFGs, by design of these surveys (*K*-band selection with no SFR cut for the GNIRS+SINFONI sample, M_* selection with very low SFR $< 1 M_* \text{ yr}^{-1}$ cut and typically long integrations for KMOS^{3D}). The median sSFR/sSFR(ms) and sizes are ≈ 1.7 times lower than for SFGs in the same M_* interval. A similar trend is seen among the $H\alpha$ -detected subset and for the objects included in the present work, although with smaller differences relative to the SFG population.

To summarize, the high $H\alpha$ detection rate of the full KMOS^{3D}, SINS/zC-SINF, LUCI, and GNIRS+SINFONI samples, and the similarity in ranges and median properties (sSFR, size) of the $H\alpha$ -detected objects as well as of those entering the sample studied here compared to the underlying population of SFGs, indicate that our sample probes well the SFG population at similar redshift and above $\log(M_*/M_\odot) > 10.3$. In the lowest M_* bin, our sample preferentially includes objects toward larger sizes and higher sSFRs, but this bias is unlikely to affect the main findings about the changes in emission line profile and outflow properties discussed in the following sections, which occur around $\log(M_*/M_\odot) \sim 10.9$ and are thus well enough sampled by the three higher M_* bins. When including the population of massive galaxies well below the main sequence of SFGs, into the regime of quenching/quiescent galaxies, the $H\alpha$ detection fractions drop most significantly (though they are still around $\sim 60\%$ in the highest M_* bin) and our sample may not yet probe the bulk of that population in terms of emission line properties—unsurprisingly given the nature and very low SFRs of these galaxies.

2.2. Data Analysis

The observations and data reduction procedures are presented by Förster Schreiber et al. (2009; N. M. Förster Schreiber et al. 2014b, in preparation) for the SINS/zC-SINF SINFONI data, by Wisnioski et al. (2014) and Davies et al. (2013) for the KMOS data, by Wuyts et al. (2014a) and E. Wuyts et al. (2014b, in preparation) for the LUCI sample and the SINFONI data of the lensed J0901+1814, and by Kriek et al. (2007) for the GNIRS+SINFONI data, to which we refer the reader for details. We focus here on the analysis of the reduced data.

For the SINFONI and KMOS data sets from the SINS/zC-SINF and KMOS^{3D} surveys, the SINFONI observations of J0901+1814 and SDSS1030–2026, and the LUCI slit-mapping data of EGS13011166, we followed the methodology of Shapiro et al. (2009), Genzel et al. (2011), Newman et al. (2012), and FS14a. The fully reduced data cubes were first median-subtracted (to remove continuum emission, which is well detected in most of the more massive SFGs of our sample), and 4σ clipped blue- and redward of the $H\alpha$ + $[\text{NII}]$ emission complex to remove OH sky emission line shot noise. In a few cases where an OH sky line was very close to the narrow (star-formation-dominated) $H\alpha$ emission, we interpolated over one to three spectral channels to remove the OH noise. The cubes were then spatially smoothed with a Gaussian of FWHM between 2 and 4 pixels (depending on S/N, source, and beam size), and then a single Gaussian line profile was fitted for each pixel to extract a smoothed velocity field of the galaxy. This velocity field was then applied in reverse to the original data cube to remove large-scale velocity gradients from orbital motions. This technique minimizes the impact of velocity broadening due to orbital motions in the final extracted spectra, and at the

same time improves the S/N for detecting faint features and line wings. The method is somewhat questionable in compact sources with unresolved strong velocity gradients, as it cannot then remove the gradients, which instead result in increased central velocity dispersions.

From the velocity-shifted cube for each galaxy, we extracted a spectrum in an aperture of diameter $\sim 0''.3$ – $0''.4$ (for AO data with $0''.05$ pixels) to $0''.6$ (for seeing limited data with 0.125 – $0''.2$ pixels) centered on the kinematic centroid, which coincides with the continuum peak for almost all of the SFGs in the highest mass bins. For galaxies in the two lower mass bins, there is often no or only a weak nuclear concentration of continuum light, consistent with the lower bulge to disk ratios found based on high-resolution *HST* imaging of these sources (Lang et al. 2014; Tacchella et al. 2014). The above aperture sizes correspond to physical radii of ~ 1.1 – 1.6 kpc (AO data) to 2.2 – 2.4 kpc (seeing-limited data) at the redshifts of our galaxies. For simplicity, throughout the paper we will refer to these spectra as “nuclear spectra” although they cover the nuclear and circum-nuclear emission of the galaxies. We also extracted outer “disk spectra” outside the nuclear aperture, over a region with significant $H\alpha$ emission. The final nuclear and disk spectra for each galaxy were normalized to a peak amplitude at $H\alpha$ of unity and interpolated onto a common velocity sampling of 30 km s^{-1} .

The quality of the spectra extracted from the data cubes above is good to excellent, owing to on-source integration times varying between 2 hr and 23 hr, with an average and median of about 8 hr. The median S/N per spectral element of the nuclear and disk spectra is ~ 10 .

For the slit spectroscopy obtained with LUCI, and the published GNIRS+SINFONI data of Kriek et al. (2007), we used the source-integrated spectra as proxies of the nuclear emission. Whereas this choice implies a potentially larger contribution from the disk regions to the nuclear spectra, inspection of the two-dimensional LUCI slit spectra and of the SINFONI $H\alpha$ maps of Kriek et al. (2007) indicates that the bulk of the line emission originates from the central regions. The impact on the co-added spectra discussed below and in subsequent sections is, however, small since these 18 LUCI and GNIRS+SINFONI spectra represent only $\approx 15\%$ of all our data sets (or 20% and 27% in the two highest mass bins), and because of their typically lower than average S/N they are substantially down-weighted in the co-adding (see below).

In constructing the various co-added spectra we used two approaches. In one approach, we gave all galaxies the same statistical weight, but left out a few lower-S/N galaxies in the sample. This choice obviously does not optimize the S/N of the co-added spectrum but instead yields the most likely “average” spectrum of the chosen subsample, and is least affected by outliers. In the second approach we gave each galaxy a weight proportional to its signal to noise ratio, to generate the best quality co-added spectrum. We did not pursue a weighting proportional to S/N^2 , as this would have given overly strong emphasis to a few galaxies with the best S/N. We also compared results by splitting up the subsample comparing their properties. We find that these different methodologies make little difference in the resulting spectra, demonstrating that the properties of our co-added spectra, at least for subsamples of 5–10 galaxies, are robust. For these reasons we chose in the end, for the display of co-added spectra and quantitative analyses the S/N-weighting scheme (with one exception, see Section 3.1). The final co-added spectra were re-binned to 40 km s^{-1} , roughly representing two

samples per average intrinsic instrumental FWHM resolution of SINFONI, KMOS, and GNIRS.

Motivated by the earlier analysis of Genzel et al. (2011), we used multiple Gaussian fitting for the spectral analysis, with the following input assumptions:

1. the systemic velocities and widths of the narrow $H\alpha$, [N II] and [S II] line components are the same, and likewise for the broad components;
2. the ratio of [N II] $\lambda 6548/\lambda 6583$ is 0.32 (Storey & Zeippen 2000); and
3. the flux ratio [S II] $\lambda 6716/\lambda 6731$ in the broad component (if detected) is ~ 1 , similar to that found in the narrow component in almost all of our SFGs and near the low-density limit.

This leaves then the following free fitting parameters: the FWHM line widths of the narrow and the broad components (Δv_{narrow} , Δv_{broad}), the velocity shift between their centroids (δv_{broad}), the flux ratios [N II] $\lambda 6583/H\alpha$ in the narrow and broad components and $H\alpha_{\text{broad-}}/H\alpha_{\text{narrow}}$, and, in cases where the [S II] lines were fitted as well, the flux ratios [S II] $\lambda 6716_{\text{narrow}}/H\alpha_{\text{narrow}}$, [S II] $\lambda 6716_{\text{narrow}}/[S II] \lambda 6731_{\text{narrow}}$, and [S II] $\lambda 6716_{\text{broad}}/H\alpha_{\text{narrow}}$. All narrow and broad Gaussian components were always fit simultaneously.

As will be seen from the discussion below (see also Genzel et al. 2011), the assumption of Gaussian line shapes is well justified for the narrow component (in terms of the central limit theorem of many individual H II regions contributing to the final shape where large velocity gradients have been removed). This justification is less obvious for the broad component, which in some cases appears to exhibit a blue/red asymmetry, in which case the inferred line widths serve as a first order description. When splitting the sample into more numerous, and smaller subsamples, or analyzing the lowest mass bin, the S/N of the broad emission can become marginal for quantitative fitting of its width. In this case, and motivated by the fairly constant velocity width of the broad component in the disk and lower mass bins (see also Newman et al. 2012), we adopted $\Delta v_{\text{broad}} = 380 \text{ km s}^{-1}$ as a fixed input parameter. For the faintest low-mass galaxies with weak [N II] emission, we also assumed that the [N II] $\lambda 6583/H\alpha$ flux ratio in the broad component was twice that in the narrow component, motivated by the findings at higher masses.

3. RESULTS

The discovery observations of FS14a raised three key issues we wish to explore in this paper. How common are the (circum-) nuclear ionized outflows? How do their outflow rates and outflow velocities vary with location of the SFG in the stellar-mass-specific SFR plane, and with redshift? What drives and excites these outflows, AGNs or (circum-)nuclear starbursts?

Tackling these questions requires a much larger sample of galaxies than was available to FS14a, and is now possible with the new high quality AO and seeing limited data sets assembled in this paper, comprising 110 SFGs with $\log(M_*/M_\odot) = 9.4\text{--}11.7$. In particular, in the two highest mass bins this sample increases the data set used by FS14a from 13 to 74 SFGs. The extended sample also covers the distribution of the main sequence of SFGs in the $\log M_*\text{--}s\text{SFR}$ plane more homogeneously (especially at $\log(M_*/M_\odot) > 10.3$) and pushes the coverage at the highest masses to specific SFRs significantly below the main sequence as can be seen in Figure 1 (see also Table 1). Moreover, our new sample includes 29 SFGs at

$z = 0.8\text{--}1.6$ and 81 at $z = 2\text{--}2.5$ (blue circles and red squares in Figure 1), allowing us to investigate the frequency and properties of nuclear outflows at lower redshifts compared to the FS14a study.

3.1. Detection of Broad Nuclear Components

In 34 of the 110 SFGs of our sample we detect a significant broad component in their individual nuclear spectra; the spectra of these 34 SFGs are plotted in Figure 2. We identify a “broad component” detection when the broad component emission flux is significant based on the uncertainties from the multiple simultaneous Gaussian fits (described in Section 2.2). We have shown previously that the assumption of Gaussian line profiles (of typically $\text{FWHM} \sim 140 \text{ km s}^{-1}$) is empirically well justified for individual giant star-forming clumps (Genzel et al. 2011). After removal of large-scale velocity gradients, our spatially resolved SINFONI and KMOS data show that also the galaxy wide spectra are near Gaussian with FWHM line widths ranging between 150 and 320 km s^{-1} . The underlying excess broad components in the spectra of Figure 2 have FWHM ranging from 430 to 5300 km s^{-1} .

Does such an excess “broad component” necessarily imply a separate broad component, or could it also be the result of beam-smearing unresolved orbital motions, especially for the seeing limited data sets? The wings of the instrumental spectral profile of the SINFONI instrument are negligible compared to the line widths of the broad (and narrow) components discussed here (Genzel et al. 2011; FS14a). The same can be said about the KMOS and GNIRS instruments. LUCI has a more complex spectral response function but the statement above still holds for the SFGs discussed here. To explore the issue of spatial “cross talk” we consider an illustrative case of a SFG with a size and mass representative of the disks observed in the SINS/zC-SINF and KMOS^{3D} surveys (Förster Schreiber et al. 2009; Mancini et al. 2011; Newman et al. 2013; Wisnioski et al. 2014). We set up an inclined ($\sin(i) = 0.76$) exponential disk (of effective radius $R_e \sim 6.5 \text{ kpc}$), plus bulge model with a total stellar mass of $M_* = 1.5 \times 10^{11} M_\odot$, and a fairly flat projected rotation curve of $v_{\text{max}} \sim 240 \text{ km s}^{-1}$, which we then convolved with a seeing limited PSF of $\text{FWHM } 0''.55$, added appropriate Gaussian noise (comparable to our SINFONI and KMOS data), and assumed [N II]/ $H\alpha = 0.3$. We then analyzed the model data cube in the same manner as for the real data, including the de-shifting of the large-scale velocity gradients, extraction of inner and outer disk aperture spectra, etc. The extracted disk spectrum ($\text{FWHM} \sim 160 \text{ km s}^{-1}$) of this model galaxy is shown in the left panel of Figure 3. The equal weight average of the outer disk spectra of 43 high-quality SFGs throughout the full mass range of our sample is shown in blue, and in green is the best-fit broad component for that spectrum. It is obvious that beam-smearing orbital motions even in a massive SFG galaxy cannot account for the broad emission in the average outer disk spectra of our sample. For main-sequence SFGs as observed in our SINS/zC-SINF and KMOS^{3D} surveys (or other SFG samples observed with near-IR integral field spectrographs, e.g., Law et al. 2009; Épinat et al. 2009, 2012), this statement is conservative since the orbital motions in most of the galaxies would be smaller than in the massive model system we used. The central $0''.3\text{--}0''.4$ diameter aperture spectrum of our model galaxy has a FWHM of 440 km s^{-1} . While the beam smearing of unresolved nuclear motions could contribute to, or perhaps even dominate a nuclear width of $\sim 400 \text{ km s}^{-1}$ in a massive SFG galaxy, it obviously cannot account for $\sim 1000 \text{ km s}^{-1}$

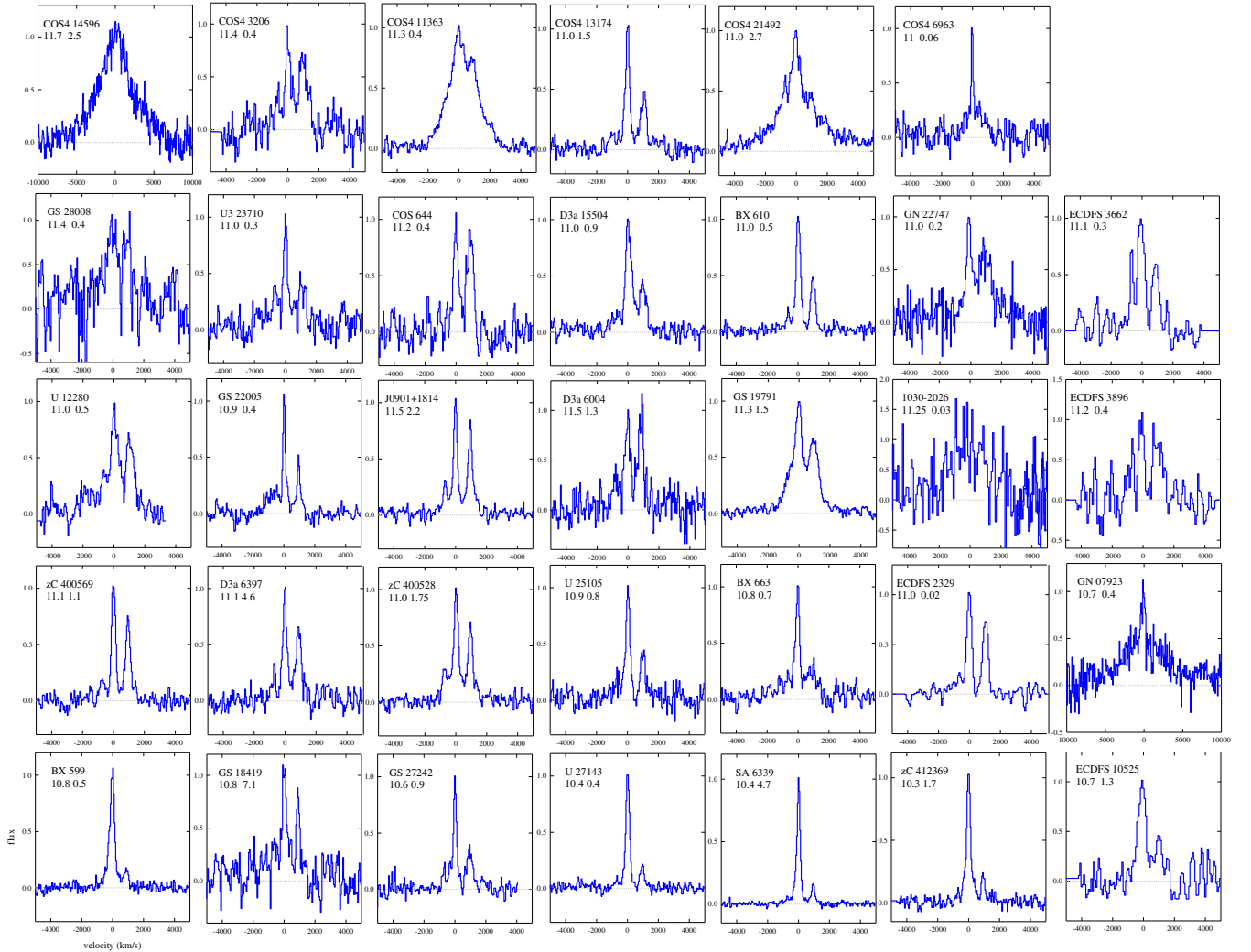


Figure 2. Individual nuclear spectra (extracted in apertures of FWHM 0.3–0.4 for AO data and 0.6 for seeing limited data) for the 34SFGs with a firm detection of a broad component at the nucleus (quality “1” or “2” in Column 7 of Table 1).

(A color version of this figure is available in the online journal.)

components we observe for the $\log(M_*/M_\odot) > 10.9$ galaxies as described below.¹⁴ The same conclusions apply for the SINFONI+AO data; while the core of the AO PSF has a narrow FWHM ≈ 0.2 , it exhibits significant broad wings with a FWHM ~ 0.55 corresponding to the uncorrected seeing (FS14a; N. M. Förster Schreiber et al. 2014b, in preparation).

In practice, a broad component can be detected in individual spectra if its integrated flux is at least 10% of the narrow component, and its width is at least twice that of the narrow component. The average S/Ns of our spectra are comparable across the stellar mass range covered, thus making the same relative broad line fraction as easy or difficult to detect at $\log(M_*/M_\odot) \sim 10$, as at $\log(M_*/M_\odot) \sim 11.3$. We have verified this assessment quantitatively by adding model broad components of FWHM 500 and 1500 km s^{-1} in H α and the [N II] lines in various strengths to the stacked central and outer disk spectra in the different

mass bins (leaving out those stacks with strong detected broad components), and then analyzing the spectra in the same manner as described in Section 2.2. In these stacks (of typically 8–11 galaxies each) the minimum detectable broad component, in the sense of a significant/correct extraction of its width and flux, is about 15%–20% of the narrow component in terms of flux ratio, more or less flat across the mass range sampled by our data and similar for both widths. These detection limits are shown as thick black and magenta lines in the right panel of Figure 3. Weaker broad components (to about 10% of the narrow flux) can still be detected but their inferred properties are uncertain.

In terms of these definitions, a significant intrinsic broad nuclear component is present in each of the 34 SFGs in Figure 2. This broad component obviously varies greatly from source to source in width and strength relative to the narrow H α and two [N II] lines. We will return to the detailed properties of this broad emission when we analyze the high quality co-added spectra.

In addition to these “firm” detections (labeled as quality “1” or “2” in Column 7 of Table 1), there are 13 “candidates” (labeled as quality “0.5” in Column 7 of Table 1) with possible but individually marginal broad nuclear components. Broad components are also detected in the outer “disks” of a number

¹⁴ Dense compact quiescent galaxies at $z \sim 1$ –3, with stellar masses of $\log(M_*/M_\odot) \sim 11$ and effective radii ~ 1 kpc have typical stellar velocity dispersions of 300 – 400 km s^{-1} (e.g., van Dokkum et al. 2009; Bezanson et al. 2013; van de Sande et al. 2013; Belli et al. 2014). Although we cannot exclude that star-forming progenitors of such very dense “cores” may be present among our galaxies and cause FWHMs up to $\sim 100 \text{ km s}^{-1}$, these are very rare and unlikely to dominate our sample (e.g., Tacconi et al. 2008; Nelson et al. 2014).

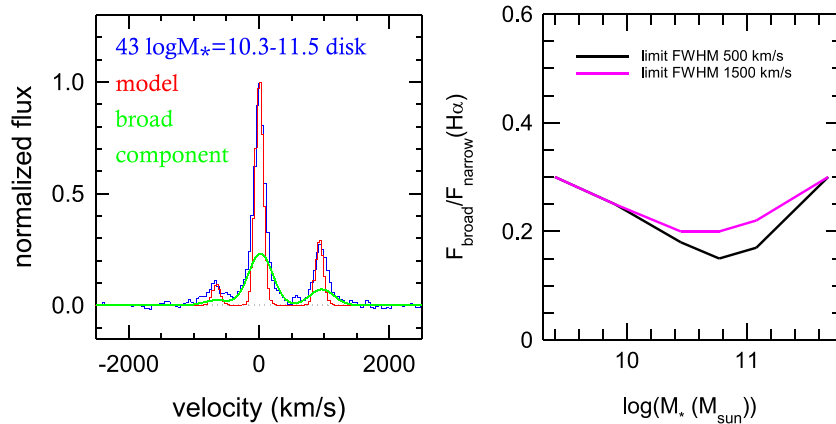


Figure 3. Left: average outer disk spectrum of SFGs with $\log(M_*/M_\odot) = 10.3\text{--}11.5$, from an equal weight co-add of 43 galaxies (blue), along with the best-fit broad component in $H\alpha$ + $[N\text{II}]$ (green), which has $\text{FWHM} \sim 400\text{ km s}^{-1}$. The red spectrum represents a massive model galaxy with a bulge and a disk ($M_{\text{total}} = 1.5 \times 10^{11} M_\odot$), resulting in a fairly flat intrinsic rotation curve of $v_{\text{rot}} \sim 240\text{ km s}^{-1}$, observed at inclination 52° . The model data cube was convolved with a FWHM angular resolution of $0''.55$ and an FWHM spectral resolution of 100 km s^{-1} , and then analyzed in the same way as our SINFONI and KMOS data, removing the large-scale velocity gradients from the rotation pixel-by-pixel and then extracting an outer disk spectrum at $R > 0''.4$. The simulated spectrum has a $\text{FWHM} \sim 160\text{ km s}^{-1}$, but is clearly much narrower than the average disk spectrum of our sample. Since the model galaxy’s mass and rotation velocity is at the upper bound of our sample, the red spectrum indicates the maximum impact of residual beam-smearing rotation even in the seeing limited KMOS^{3D} and SINS/zC-SINF data sets. The broad emission in the disk spectrum thus must come from a gravitationally unbound component, as proposed earlier (Shapiro et al. 2009; Genzel et al. 2011; Newman et al. 2012). Right: limits for detection (and correct parameter extraction) of broad components of $\text{FWHM } 500\text{ km s}^{-1}$ (black) and 1500 km s^{-1} (pink) as a function of stellar mass, in the SFG stacked spectra analysed in this paper. These limits were derived by inserting Gaussian model components of different amplitudes and widths into the disk/nuclear co-added spectra (without significant broad components) and re-extracting their properties from six component Gaussian fits. (A color version of this figure is available in the online journal.)

of our SFGs, as previously discussed in Genzel et al. (2011) and Newman et al. (2012). However, in these cases the extended broad component in $H\alpha$ and $[N\text{II}]$ typically has a FWHM of $\sim 380\text{ km s}^{-1}$, about twice that of the narrow component.

We note that because a majority of the data sets considered here (80 of 110) were obtained in natural seeing (and 18 of them consist of source-integrated spectra), the fraction of galaxies in which we identify a broad nuclear emission component may represent a lower limit. Indeed, due to the more significant effects of beam-smearing in seeing-limited data, broad nuclear emission may be more easily outshined, or diluted, by emission from the disk regions (see also discussion by FS14a).

3.2. Spectral Properties of the Broad Nuclear Emission

3.2.1. Line Widths, Velocities and Flux Ratios

To determine the average properties of the nuclear emission we co-added spectra of different subsamples, keeping in mind the substantial variation of profiles seen in the individual sources in Figure 2. Following FS14a we started by averaging the individual spectra of all 31 galaxies in the highest mass bin at $\log(M_*/M_\odot) \geq 10.9$ that have firm or candidate individual detections of a broad nuclear component (quality criteria 0.5, 1, or 2 in Column 7 of Table 1). We excluded here (as elsewhere below) the spectra of the candidate BLR sources. We weighted each spectrum by its S/N given in Column 6 of Table 1. This stacked spectrum is shown in the left panel of Figure 4 (gray line), and exhibits a prominent broad emission component (blue line, after subtraction of the narrow emission (gray) from the multi-Gaussian fits to the stacked spectrum as described in Section 2.2) with wings extending to 2000 km s^{-1} to the blue and the red relative to the narrow $H\alpha$ emission. The corresponding stacked outer disk spectrum of SFGs in the same mass bin, plotted in the middle panel of Figure 4 (gray line), also shows a broad component (blue line), but of much smaller width ($\text{FWHM } 400\text{--}500\text{ km s}^{-1}$ in $H\alpha$), demonstrating

that the very broad component indeed only occurs on average in the central regions. The multi-Gaussian component fit to the nuclear spectrum shows that the broad nuclear component has a FWHM of $1710 \pm 70\text{ km s}^{-1}$ in $H\alpha$ and $[N\text{II}] \lambda\lambda 6548/6583$ (indicated by the red and green lines in the left panel of Figure 4, respectively). The narrow $[N\text{II}] \lambda 6583/H\alpha$ flux ratio is 0.55 ± 0.02 and the broad to narrow $H\alpha$ flux ratio is 0.37 ± 0.08 . The broad $[N\text{II}] \lambda 6583/H\alpha$ ratio is about five times larger than the narrow ratio, 2.7 ± 0.7 ; the strong broad $[N\text{II}]$ emission thus dominates the overall broad emission component and explains its overall asymmetric shape with a strong redshifted peak and a long blueshifted wing (see FS14a).

The broad emission is also confidently detected at 9σ in the $[S\text{II}] \lambda\lambda 6716/6731$ lines, as shown in the right panel of Figure 4 (blue line). The broad to narrow $[S\text{II}]$ line flux ratio is $0.102 (\pm 0.015)$, and the ratio of the narrow $[S\text{II}] \lambda 6716$ to $H\alpha$ ratio is $0.12 (\pm 0.01)$. However, the exact value of these ratios depends also on the broad flux ratio of $[S\text{II}] \lambda 6716/\lambda 6731$, which cannot be uniquely constrained from the data, and which we assumed to be ~ 1 , motivated by the ratio in the narrow $[S\text{II}]$ lines. All these values are summarized in Table 2, are in excellent agreement with FS14a, and are quite robust to the sample selection. Changing the sample to include only the best individual detections of nuclear broad emission, or stacking all 35 SFGs with $\log(M_*/M_\odot) > 10.9$, or extending the lower mass limit to 10.6, all yield a broad profile with $\text{FWHM} \sim 1300\text{--}1800\text{ km s}^{-1}$ in each $H\alpha$, $[N\text{II}]$, and $[S\text{II}]$, which is dominated by strong broad $[N\text{II}]$ emission.

A possible alternative, and formally also acceptable decomposition of the specific co-added nuclear spectrum in the left panel of Figure 4 is obtained if one assumes that the broad emission is due to $H\alpha$ only, as would be expected for BLR emission (see Netzer 2013). For the three candidate BLR sources in our sample (GOODSN-07923, COS4-14596 and COS4-21492) this explanation may indeed be fully appropriate. These three sources have the largest broad line widths ($\text{FWHM } 5300, 5200,$

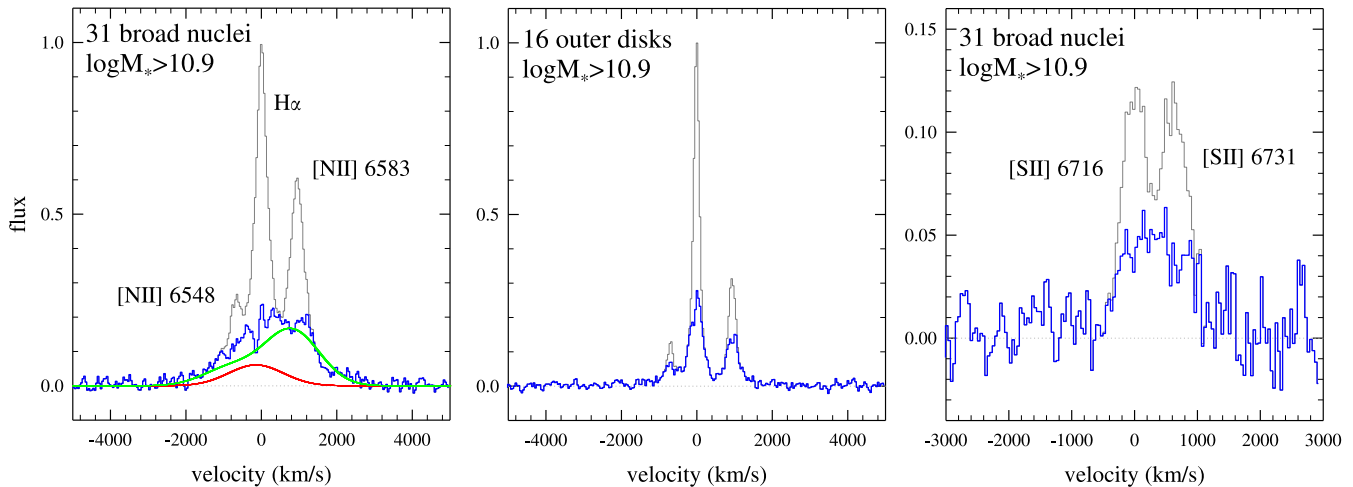


Figure 4. Left panel: co-added $H\alpha$ -[N II] spectrum (weighted by signal-to-noise ratio) of the 31 $\log(M_*/M_\odot) = 10.9$ –11. Seven nuclei with individual, firm, and candidate broad emission detections (gray), but excluding the two nuclei with broad line regions. The blue line denotes the broad component, after removal of the narrow $H\alpha$ /[N II] lines, from a six-parameter Gaussian fit. The thin dotted red and green curves show the $H\alpha$ and [N II] broad fit components separately. Middle panel: average outer disk spectrum (gray) for those 16 (of the 31) $\log(M_*/M_\odot) \geq 10.9$ SFGs for which significant extended $H\alpha$ emission is detected, weighted again by S/N. As in the left panel, the blue profile denotes the residual broad emission component. Right panel: co-added [S II] spectrum (gray) of the 31 nuclei. As in the other panels, the blue profile denotes the [S II] broad component, after removal of the narrow [S II] $\lambda\lambda 6716+6731$ emission, assumed to have the same width and central velocity as the $H\alpha$ /[N II] lines.

(A color version of this figure is available in the online journal.)

Table 2
Spectral Properties of $\log(M/M_\odot) > 10.9$ Stacks

Property	Narrow Component	Broad Component
Δv (FWHM) (km s^{-1})	center (31 objects): 365 (6) disk (16 objects): 160 (4)	1711 (70) 440 (30)
δv_{broad} (km s^{-1}) ^a	center:– disk:–	–130 (40) 11 (8)
$F(H\alpha)_{\text{broad}}/F(H\alpha)_{\text{narrow}}$ ^b	center:– disk:–	0.4 (0.1) 0.85 (0.1)
$F(\text{[N II] } \lambda 6583)/F(H\alpha)$	center: 0.55 (0.13) disk: 0.23 (0.02)	2.7 (0.7) 0.7 (0.06)
$F(\text{[S II] } \lambda\lambda 6716+6731)/F(H\alpha)_{\text{narrow}}$	center: 0.27 (0.03) disk: 0.2 (0.03)	0.2 (0.03) 0.12 (0.03)
$F(\text{[S II] } \lambda 6716)/F(\text{[S II] } \lambda 6731)$	center: 1.07 (0.08) disk: 1.13 (0.1)	~ 1
$F(\text{[O I] } \lambda 6300)/F(H\alpha)_{\text{narrow}}$	0.099 (0.025) for best 6	...
$F(5007 \text{ [O III]})/F(H\beta)_{\text{narrow}}$	4 (–1, +4) for best 6	...

Notes. Values given in parentheses are the uncertainties of the measurements.

^a Velocity offset between the centroid velocity of the broad component relative to the narrow component.

^b Ratio of the integrated $H\alpha$ flux in the broad and narrow components.

and 2500 km s^{-1}) and at the same time do not show evidence for narrow (or broad) [N II] or [S II] emission, suggesting that in these cases the line emission is indeed dominated by very dense gas from a classical, virialized BLR very close to the central massive black hole (see Netzer 2013). For the co-added nuclear spectrum in Figure 4, however, the broad emission of $\text{FWHM} \sim 2200 \text{ km s}^{-1}$ would then be redshifted by $\sim 310 \text{ km s}^{-1}$ relative to the narrow $H\alpha$, [N II], and [S II] emission. In this explanation the broad $H\alpha$ emission would have to come from a BLR in most SFGs entering into the co-added profile. Such a large shift between the broad and narrow $H\alpha$ lines for most or all galaxies is highly unlikely, when compared to local SDSS AGN results (Bonning et al. 2007; Liu et al. 2014; Mullaney et al. 2013). Probably the most conclusive argument

against a BLR explanation for the majority of our sources is the clear detection of a broad [S II] line in the co-added spectrum and in individual sources, with the same width as for the $H\alpha$ and [N II] lines (right panel of Figure 4), and with a centroid velocity consistent with that of the narrow emission. Of course, for those of our SFGs with spatially resolved broad nuclear emission a BLR explanation is excluded in any case.

Another decomposition with the broad [N II] emission having the same [N II]/ $H\alpha$ ratio as in the narrow component is also possible but is less likely for the nuclear spectrum in Figure 4 (and other stacks discussed below), since the broad [N II] $\lambda 6548$ emission is weaker and cannot help explaining the strong blue excess in the wings of the overall broad emission in Figure 4. This then would result in a very asymmetric line profile of the broad emission, as well as a poorer fit to the data (see FS14a).

In summary of this section, we fully confirm in a much larger sample the discovery of FS14a that the most massive near-main sequence SFGs at $z \sim 1$ –3 frequently exhibit a very broad nuclear component that is present in $H\alpha$, [N II], and [S II] emission lines, and is much wider than in the outer disk regions of the same galaxies. Combined with the evidence that the broad emission is spatially resolved ($\text{FWHM} \sim 2$ –3 kpc) in four to five of these SFGs (FS14a, Wuyts et al. 2014a) and that the broad emission is present in the forbidden lines of [N II] and [S II], we have a compelling case that the broad emission represents a powerful nuclear outflow. The blueshift of the broad $H\alpha$ emission relative to the narrow emission in Figure 4 ($-130 (\pm 40) \text{ km s}^{-1}$, second row and second column of Table 2) is also consistent with an outflow interpretation, because of the plausible presence of internal differential extinction (Genzel et al. 2011).

3.2.2. Line Ratios and Constraints on the Excitation Mechanisms

We next explore the mechanism(s) exciting the broad nuclear line emission, based on rest-optical diagnostic line ratios (e.g., Baldwin et al. 1981; Veilleux & Osterbrock 1987). Figure 5 shows the line ratio properties derived from the

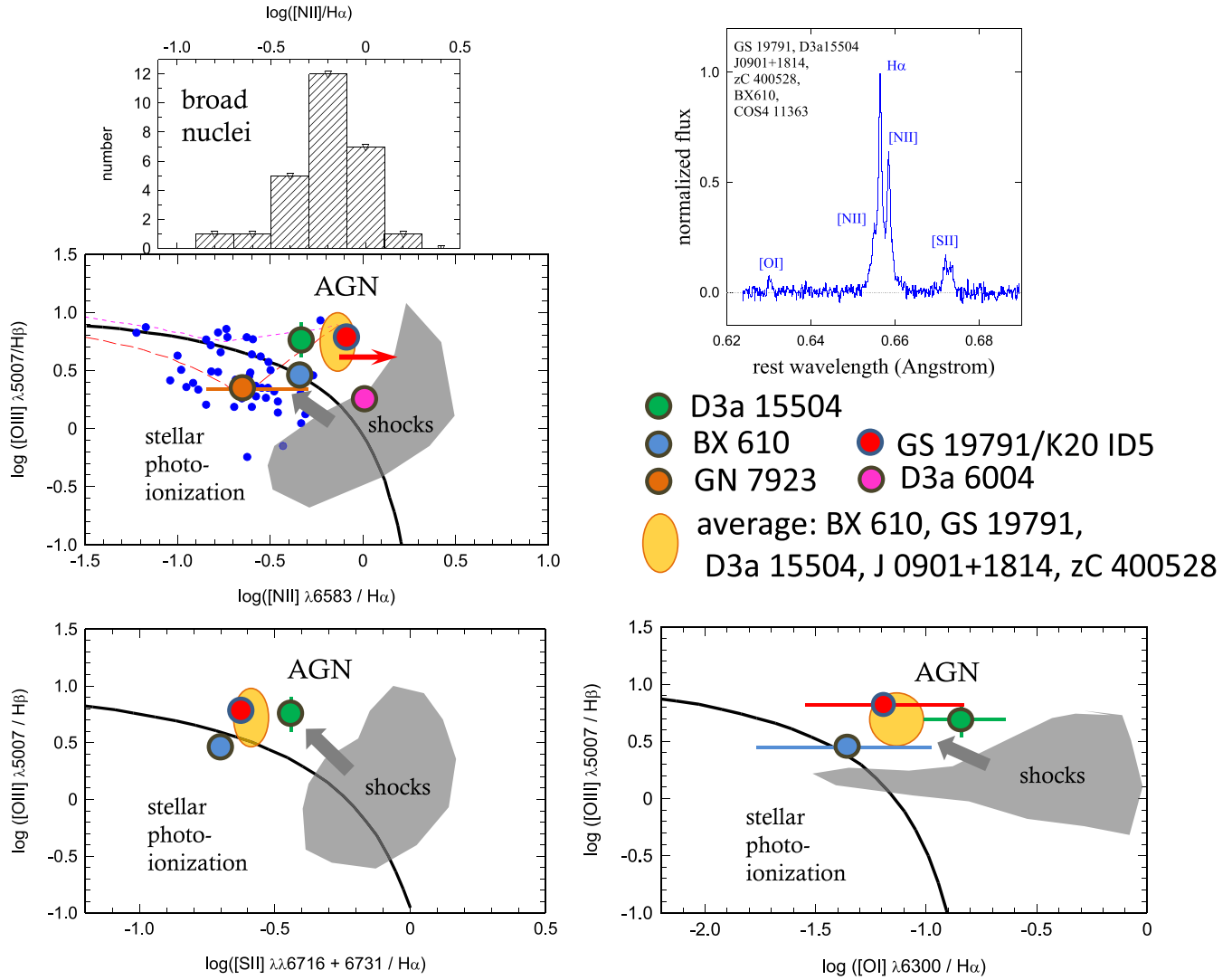


Figure 5. Diagnostic line ratio diagrams for the nuclear broad line SFGs in our sample. The three nuclei of GS3–19791, D3a–15504, and BX 610 have detections in all four ratios $[\text{N II}] \lambda 6583/\text{H}\alpha$, $[\text{O III}] \lambda 5007/\text{H}\beta$, $[\text{S II}] \lambda\lambda 6716+6731/\text{H}\alpha$, and $[\text{O I}] \lambda 6300/\text{H}\alpha$ and are plotted as large red, green, and blue circles. D3a–6004 has two line ratios, but the $[\text{O III}] \lambda 5007/\text{H}\beta$ ratio refers to the galaxy as a whole. The large orange ellipse denotes the co-added spectrum of GS3–19791, D3a–15504, BX 610, J0901+1814, and zC400528 (top right panel). The red arrow pointing to the right indicates that for the broad line component, the $[\text{N II}] \lambda 6583/\text{H}\alpha$ ratio is a factor of about two larger than for the narrow component. Hatched black histograms denote the distribution of the (total) $[\text{N II}] \lambda 6583/\text{H}\alpha$ ratio in all SFGs of our sample that have a good detection of a nuclear broad component (with the exception of zC400569, see the text). The small filled blue circles are other $z \sim 1$ – 2.5 SFGs from Newman et al. (2014), Trump et al. (2013), Shapley et al. (2005), Kriek et al. (2007), and Liu et al. (2008; see also Steidel et al. 2014). The thick black line is the extremal “starburst” line from the models of Kewley et al. (2001). Sources to the left of that line can be accounted for ISM photoionized by stars. The red dashed line denotes the location of sources with a combination of a “normal photoionized ISM” and the metal rich narrow line region around the AGN. The magenta dotted line denotes the location of sources with a combination of an “extreme photoionized ISM (large ionization parameter, high density)” and a metal-rich narrow line region around an AGN (from Kewley et al. 2013). The large dark gray polygons labeled “shocks” denote the locations of gas ionized by fast shocks (200 – 1000 km s^{-1}). Gray arrows denote the direction in which gas with a combination of shocks and stellar photoionization, or with a radiative precursor would move (Dopita & Sutherland 1995; Allen et al. 2008; Sharp & Bland-Hawthorn 2010; Rich et al. 2010, 2011). Upper right panel: co-added nuclear spectrum of BX610, GS3–19791, zC400528, D3a–15504, J0901+1814, and COS4–11363 showing the detection of $[\text{O I}] \lambda 6300$ emission.

(A color version of this figure is available in the online journal.)

data of our sample and compares them with various recent excitation/ionization models (Kewley et al. 2001, 2006, 2013; Allen et al. 2008; Rich et al. 2010, 2011; Sharp & Bland-Hawthorn 2010; Newman et al. 2014). There is growing evidence that at $z \sim 1$ – 2 , the physical conditions of the interstellar medium (ISM) of SFGs are different than those of normal SFGs at $z \sim 0$ (e.g., Steidel et al. 2014). High- z SFGs exhibit an offset toward higher excitation in the classical diagrams plotting $[\text{O III}] \lambda 5007/\text{H}\beta$ versus $[\text{N II}] \lambda 6583/\text{H}\alpha$, $[\text{S II}] \lambda\lambda 6716+6731/\text{H}\alpha$, and $[\text{O I}] \lambda 6300/\text{H}\alpha$, such that the criteria to distinguish pure stellar photoionization from AGNs and/or shock excitation

devised based on normal $z \sim 0$ SFGs may not be directly applicable at higher redshift (e.g., Kewley et al. 2013 and references therein). Measurements have been published for $[\text{O III}] \lambda 5007/\text{H}\beta$ versus $[\text{N II}] \lambda 6583/\text{H}\alpha$, showing that normal, non-AGN SFGs occupy the region between the locus of normal local SFGs and H II regions, and the theoretical “maximum starburst line” from Kewley et al. (2001), overlapping with the location of nearby starburst systems (e.g., Shapley et al. 2005; Kriek et al. 2007; Liu et al. 2008; Trump et al. 2013; Steidel et al. 2014). As illustrated in the middle left panel of Figure 5, this “extreme starburst line” (thick black curve) coincides well with the

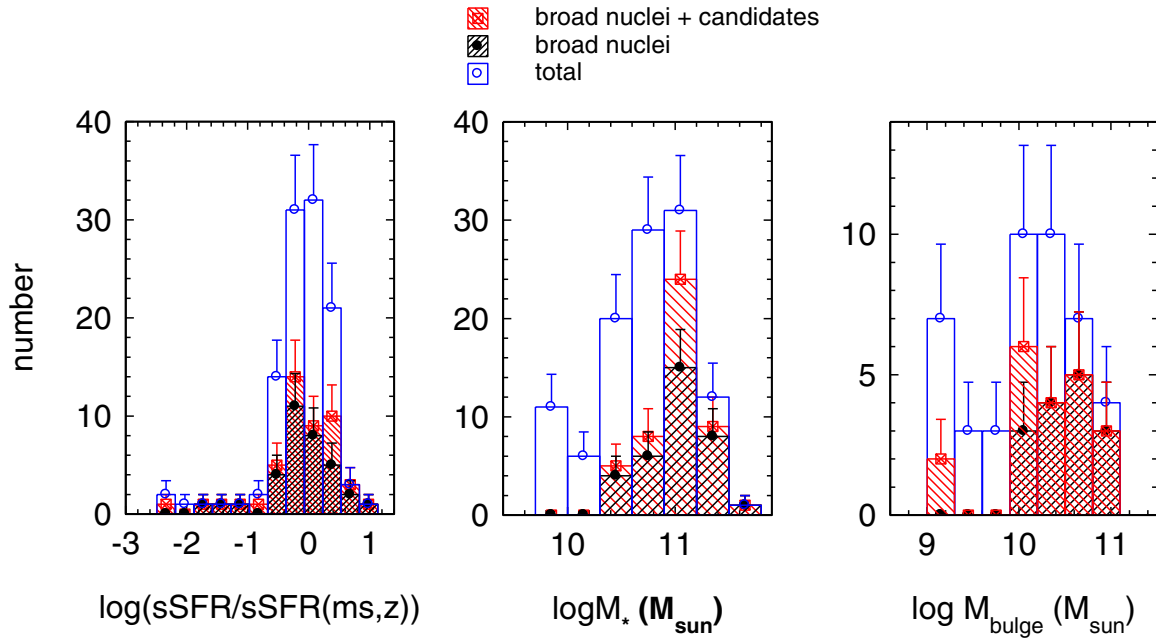


Figure 6. Number of individually detected broad nuclear components for firm detections (“quality 1 +2” in Table 1, black hatched bars, black circles, and 1σ errors), for firm plus candidate detections (“quality 0.5+1+2” in Table 1, red hatched bars), compared to all galaxies (blue bars), all as a function of logarithmic offset from the normalized main sequence line (left panel), as a function of total galaxy stellar mass (central panel) and of bulge stellar mass (right panel). The error bars are Poissonian.

(A color version of this figure is available in the online journal.)

upper envelope of pure stellar photoionization models for ISM conditions arguably more appropriate at $z \sim 1-2$. Therefore, we interpret our emission line ratios using the Kewley et al. (2001) extreme starburst line in all three diagnostic diagrams considered here.

As already found by FS14a and confirmed in the spectra of Figure 2 the nuclear spectra in the $\log(M_*/M_\odot) > 10.9$ SFGs typically have high (total) $[\text{N II}] \lambda 6583/\text{H}\alpha$ ratios ($\log([\text{N II}]/\text{H}\alpha)$ ranging from -0.7 to 0.2 , see Table 1 and histogram at the top left of Figure 5). The broad component $[\text{N II}] \lambda 6583/\text{H}\alpha$ ratios in the stack of Figure 4 and in the best individual broad line sources are even greater ($\log([\text{N II}]/\text{H}\alpha) \sim 0-0.4$). These ratios are at or above the highest values explainable by stellar photoionization for super-solar metallicity (Veilleux & Osterbrock 1987; Kewley et al. 2001, 2006, 2013). For the same spectra, the ratio of narrow $[\text{S II}]$ to $\text{H}\alpha$ flux is $\log([\text{S II}] \lambda \lambda 6716+6731/\text{H}\alpha) = -0.57 \pm 0.05$ (Table 2).

For a small subset of six broad emission sources, we also detect $[\text{O I}] \lambda 6300$ (the top right panel of Figure 5 shows the co-added spectrum) with $\log([\text{O I}]/\text{H}\alpha) \sim -1$ (Table 2). For five sources (GS3-19791, D3a-15504, Q2343-BX610, D3a-6004, GOODS-N-07923), we have $[\text{O III}] \lambda 5007/\text{H}\beta$ from seeing-limited SINFONI and LUCI observations, with source-integrated values of $\log([\text{O III}]/\text{H}\beta)$ between $+0.25$ and $+0.75$ (Newman et al. 2014). Because of the beam smearing, the source-integrated ratios are probably lower bounds to the nuclear $[\text{O III}]/\text{H}\beta$ ratios (see also FS14a).

In the diagnostic diagrams of Figure 5, the galaxies with several line ratios, as well as their averages, overall occupy the area at and above the extreme “starburst” line of Kewley et al. (2001), where the narrow line regions of metal-rich AGNs are observed to be located in the local universe, and expected to lie at higher z (Kewley et al. 2013). Of those only Q2343-BX610 could be due to pure stellar photoionization. The narrow emission of GOODS-N-07923 is fully consistent with stellar

photoionization, but its broad emission almost certainly is due to a BLR. Combining the constraints, the alternative of pure shock excitation (Dopita & Sutherland 1995; Allen et al. 2008; Rich et al. 2010, 2011; Sharp & Bland-Hawthorn 2010) also seems unlikely in these cases, with the exception of D3a-6004. For the other nuclear broad emission SFGs for which we only have $[\text{N II}]/\text{H}\alpha$ (top histogram in Figure 5), the high values also are in agreement with the best cases discussed above and favor the AGN excitation (and/or shock excitation) explanation.

Figure 5 provides convincing evidence that for those of our SFGs for which multiple line ratios are available the observed line ratios are consistent with a significant AGN contribution to the gas excitation. However, when allowing also the combination of different mechanisms it is possible to explain the observed line ratios with metal rich gas, ionized and excited by a combination of fast shocks and stellar radiation, in agreement with Newman et al. (2014). This possibility is indicated by the gray thick arrows in the diagnostic diagrams of Figure 5. As discussed by Newman et al. (2014) and FS14a, mixed contributions of different excitation mechanisms to the observed line emission could partly be attributed to beam-smearing, since even for our best resolution SINFONI+AO data, the smallest spatial scales probed are around 1–2 kpc.

3.3. Incidence and Properties of Nuclear Broad Components as a Function of Mass, Specific Star Formation Rate, and Redshift

In this section, we explore trends in the broad component emission as a function of galaxy properties and redshift. To this aim, we consider the fraction of objects with detected broad nuclear emission as a function of stellar mass, offset from the main sequence in SFR, and bulge mass, shown in Figure 6. We also derive the line profile properties of the broad component from co-added spectra of galaxies in different bins of stellar

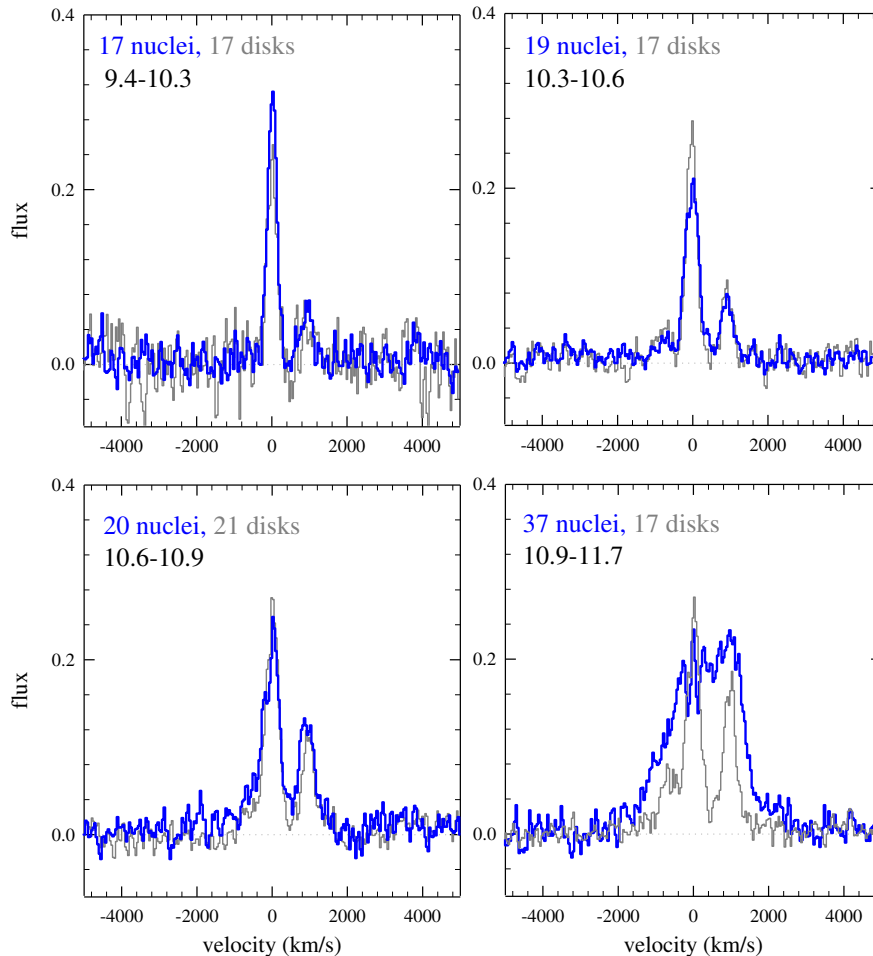


Figure 7. Properties of residual broad component spectra from S/N weighted stacking of all spectra in each of the four mass bins, after removal of the narrow component, as in Figure 4. In each panel the blue spectrum is the broad nuclear residual profile, while the gray spectrum is the outer disk broad residual profile in the same mass bin.

(A color version of this figure is available in the online journal.)

mass, sSFR, and redshift. These spectra are plotted in Figures 7 and 8, and the derived trends are shown in Figure 9. Again, the three candidate BLR sources are excluded from the analysis.

3.3.1. Correlation of the Broad Nuclear Components with Galaxy Stellar Mass

Inspection of Figure 1 shows that the *individual* firm and candidate detections of broad nuclear components cluster in the two high mass bins. This is demonstrated more quantitatively in the histogram distributions in Figure 6 (middle panel) and summarized in Table 3. Below $\log(M_*/M_\odot) = 10.3$ none of the individual SFGs shows such a broad nuclear component, and there are not even any possible candidates. Between $10.3 < \log(M_*/M_\odot) < 10.9$ the incidence of a broad nuclear component in the individual spectra is between 20 and 26 (± 10)%, depending on whether or not SFGs with candidate detections are included. Then above $\log(M_*/M_\odot) = 10.9$, 55 (± 11)% of objects show a firmly detected broad nuclear component of FWHM ~ 500 – 5200 km/s, where the quoted error bars (here and below) are the Poisson uncertainties. If the broad emission candidate sources are included, the incidence increases to 77 (± 13)%. While the quality of their individual spectra is not sufficient to classify the latter reliably, a weighted co-add of the spectra of the 10 candidates in this mass range exhibits the same properties as those of the SFGs with firmly detected broad

component emission: a broad FWHM of 610 km s^{-1} in $\text{H}\alpha$ and $[\text{N II}]$, and a narrow/broad $[\text{N II}] \lambda 6583/\text{H}\alpha$ flux ratio of ~ 0.6 . In the following we will treat the incidence of the firm detections as a conservative lower limit, but consider the average of this value and the incidence of firm and candidate detections ($66\% \pm 15\%$) as the most likely value of incidence.

As discussed in Section 3.1, the detectability of broad emission components does not vary much as a function of mass (indicated by the thick black and magenta curves in the right panel of Figure 3 and the upper right panel of Figure 9), such that a broad component of the same fraction should have been detectable throughout the stellar mass range spanned by our galaxies. Table 3 summarizes the incidence of broad components as a function of stellar mass.

We next studied the *average* profiles as a function of galaxy stellar mass, independently of whether individual profiles exhibit broad components or not, by weighted co-adding of the spectra of *all* SFGs in the nuclear regions and outer disk regions of the same galaxies, in each of the four mass bins. The resulting residual broad profiles, after removal of the narrow components in multi-Gaussian fitting (as described in Section 3.2.1) are shown in Figure 7 for both the nuclear and outer disk regions (blue and gray lines, respectively). The extracted properties of these co-added profiles in the mass bins are summarized in Figure 9.

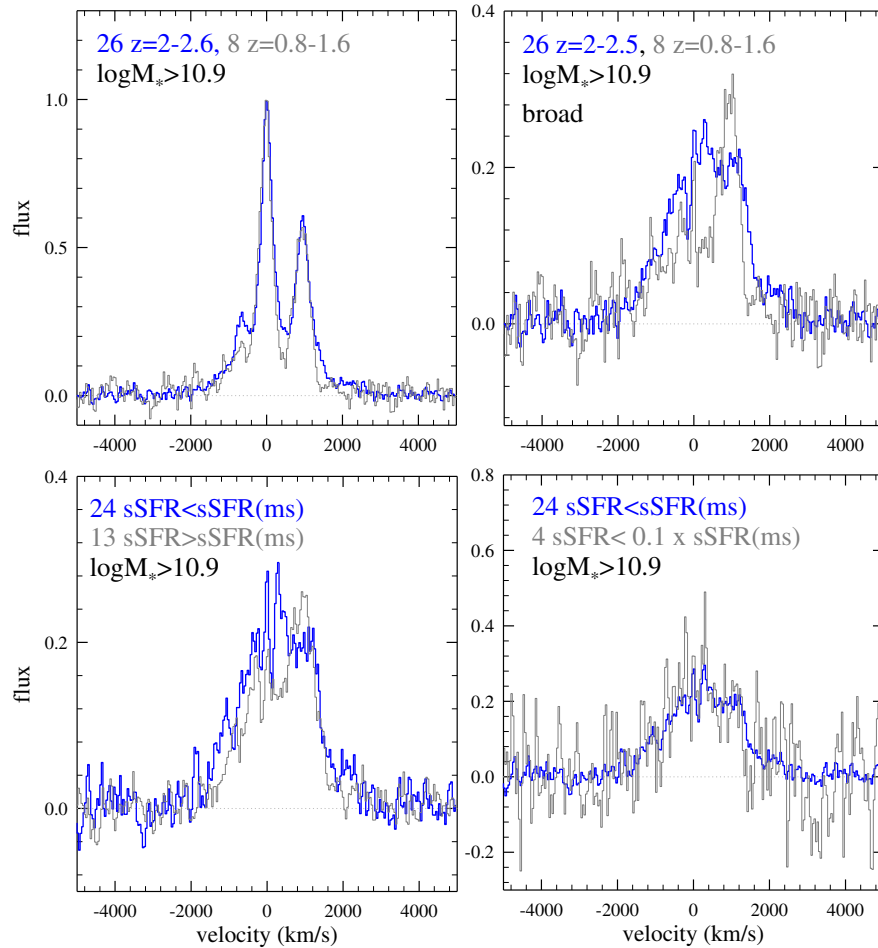


Figure 8. Top: comparison of broad nuclear spectra (individually detected, including candidates but excluding the BLR sources) at $z = 2-2.6$ (blue) and $z = 0.8-1.6$ (gray), in the mass bin $\log(M_*/M_\odot) \geq 10.9$. The left panel compares the total co-added spectra (weighted by S/N), while the right panel shows the broad components, after removal of the narrow components, as in Figures 4 and 7. Bottom left: comparison of the weighted, co-added spectra in the $\log(M_*/M_\odot) \geq 10.9$ bin, below (blue) and above (gray) the main sequence. Bottom right: comparison of the broad residual spectrum of the four galaxies with a tenth or less the specific star formation rate of the main sequence (gray) with the near- but below-main sequence stack from the bottom left panel (blue).

(A color version of this figure is available in the online journal.)

Table 3
Incidence of Broad Nuclear Emission Components and AGN

$\log(M_*/M_\odot)$	Number of SFGs	Number Broad Nuclei ^a	Number AGN	Broad Nuclei Fraction Broad ^b	AGN Fraction AGN ^c
10.9–11.7	44	24(34)	13(21)	0.55(0.77) \pm 0.12	0.38(0.51) \pm 0.11
10.6–10.9	30	6(8)	5(9)	0.2(0.27) \pm 0.09	0.15(0.37) \pm 0.09
10.3–10.6	19	4(5)	0(1)	0.21(0.26) $_{0.11}$	0(0.06) \pm 0.06
9.4–10.3	17	0	0(2)	0	0(0.15) \pm 0.11

Notes.

^a The first number denotes the number of SFGs with broad line components of quality 1 and 2 in Table 1, the number in parentheses denotes the number with quality 1 + 2 + candidates (0.5).

^b The first number denotes the fraction of SFGs (of the total in that mass bin) of broad line components of quality 1 and 2 in Table 1, the number in parentheses denotes the fraction of quality 1 + 2 + candidates (0.5). The quoted uncertainty in the subscript is the 1σ Poissonian uncertainty.

^c The first number denotes the fraction of SFGs in the common sample (of the total in that mass bin) that are firmly identified as AGNs from at least one of the AGN-identifying criteria (X-ray, mid-IR, radio or optical spectroscopy), the number in parentheses denotes the fraction of SFGs in the common sample that either are firm or candidate AGNs. The quoted uncertainty in the subscript is the 1σ Poissonian uncertainty.

The nuclear and outer disk residual broad components of the co-added spectra in Figure 7 are basically identical in the lowest two mass bins (upper panels), and even in the third mass bin ($\log(M_*/M_\odot) = 10.6-10.9$, lower left panel) the nuclear

broad component on average is only marginally wider than its outer disk counterpart. Then in the highest mass bin (lower right panel), the broad nuclear component is drastically wider than the outer disk one. This suggests that on average the broad

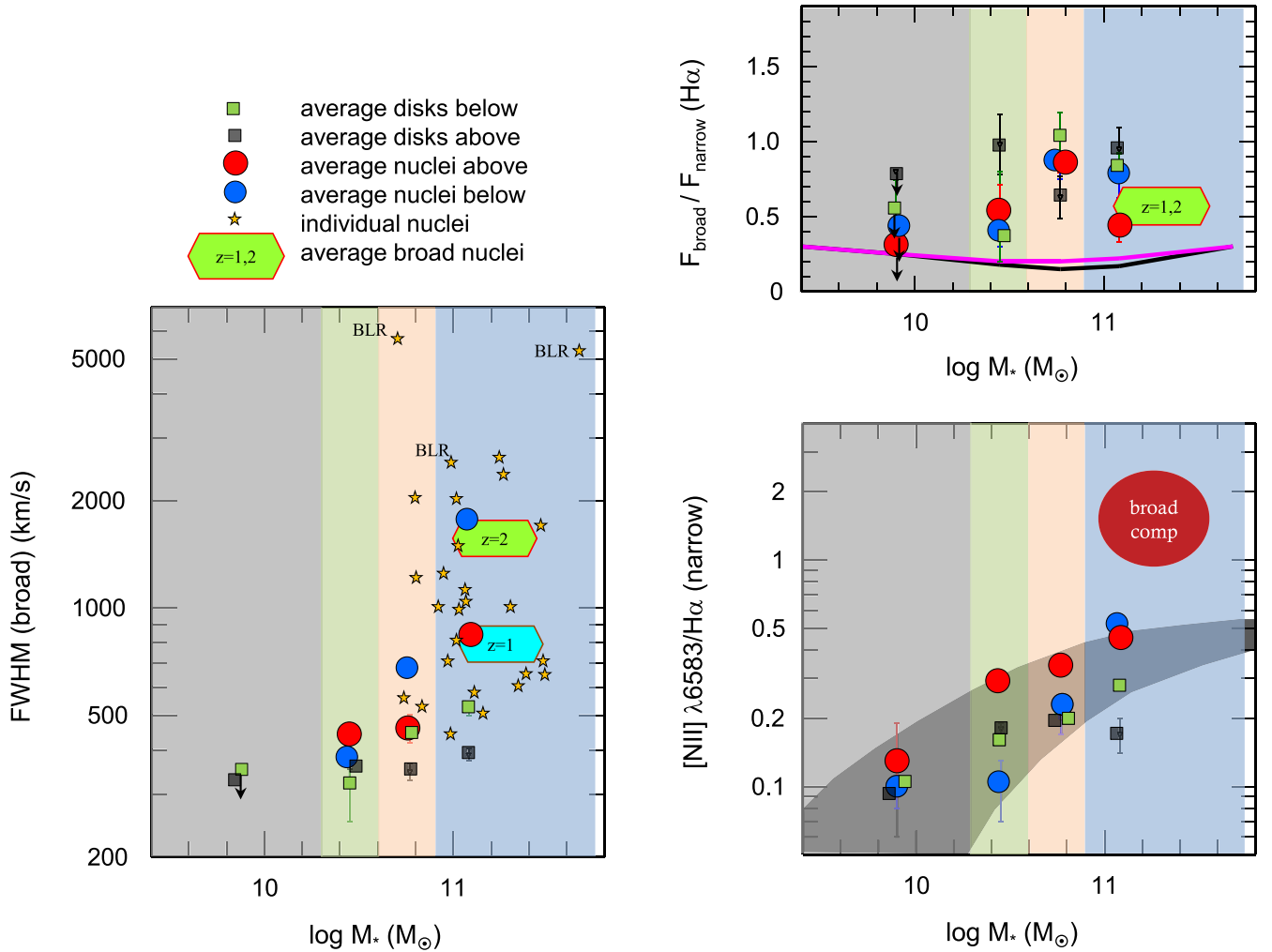


Figure 9. FWHM line width of the broad component (left), narrow and broad [N II] $\lambda 6583/\text{H}\alpha$ flux ratio (bottom right), and broad to narrow $\text{H}\alpha$ flux ratio (top right) of the nuclear and disk spectra as a function of stellar mass. Filled green and black squares denote weighted stacks in the outer disks, above and below the main sequence line respectively, in the four stellar mass bins marked by gray, green, pink, and blue shading (same as in Figure 1). Filled blue and red circles show the stacks for the nuclear regions, again above and below the main sequence line. Asterisks denote individual SFGs. Hexagons mark average of the $z = 0.8\text{--}1.6$ and $2\text{--}2.6$ SFGs. The dark gray shading in the lower right panel shows the $z \sim 1\text{--}2$ mass metallicity relation (Erb et al. 2006; Liu et al. 2008; Zahid et al. 2014; Wuyts et al. 2014a). The large brown oval marked “broad comps” and the green hexagon show the ratios of the broad $\lambda 6583$ [N II]/ $\text{H}\alpha$ lines, while all other symbols refer to the narrow component. The thick black and pink near-horizontal curves in the upper right panel denote the limits of detecting and correctly inferring the width and amplitude relative to the narrow component for a FWHM 500 and 1500 km s^{-1} broad emission component in the different stacks (same as right panel in Figure 3).

(A color version of this figure is available in the online journal.)

nuclear and outer disk components at $\log(M_*/M_\odot) = 9.4\text{--}10.9$ reflect largely the same physical process, namely modest outflow velocity ($\sim 200 \text{ km s}^{-1}$) winds driven by massive stars and supernovae throughout the entire galaxy, as discussed in Genzel et al. (2011) and Newman et al. (2012). Above $\log(M_*/M_\odot) \sim 10.9$ an entirely different physical process appears that originates only in the nuclear regions, and has much higher outflow velocities for almost all galaxies, thus completely changing the average nuclear spectrum. This is not to say that there are not a few such broad nuclear outflow sources at lower mass, but they are much rarer there, as seen from Figures 2 and 6.

3.3.2. Correlation of the Broad Nuclear Components with Bulge Stellar Mass

Next we estimated the incidence of broad components as a function of bulge mass. This is motivated by the finding of several groups that the bulge mass (or central stellar surface density), and not the total stellar mass, appears to be most

strongly correlated with the quenched (red) fraction at the high-mass tail of the $z = 0\text{--}2.5$ galaxy population (Franx et al. 2008; Cheung et al. 2012; Bell et al. 2012; Wake et al. 2012; Fang et al. 2013; Lang et al. 2014).

Lang et al. (2014) have demonstrated that it is possible to infer high- z bulge masses from spatially resolved SED modeling of multi-band optical and near-IR *HST* imagery yielding stellar mass maps, and then carrying out a two-component structural analysis. In the right panel of Figure 6, we exploit the analysis of Lang et al. (2014) and Tacchella et al. (2014) for our SINS/zC-SINF and KMOS^{3D} targets to explore the incidence of broad nuclear emission sources as a function of bulge mass. The quoted mass corresponds to that of the bulge from the best-fit two-component disk + bulge model (Sersic profiles with index $n = 1$ and $n = 4$, respectively) to the two-dimensional stellar mass distribution of the galaxies. The trend seen as a function of bulge mass is broadly similar to that as a function of total galaxy stellar mass in that there is a steep onset in the fraction

of nuclear broad emission line galaxies, which occurs at/above $\log(M_{*, \text{bulge}}/M_{\odot}) = 10$.

However, we cannot distinguish on the basis of these comparisons whether stellar mass or bulge mass (or another quantity correlated with these, such as central black hole mass) is a better predictor of the onset of a nuclear broad component, presumably because of the combination of the uncertainties in the derived bulge masses, as well as the still modest size of our sample in view of the significant scatter in inferred bulge masses at a given galaxy's stellar mass.

3.3.3. Properties of the Broad Nuclear Components as a Function of Redshift

Our sample is sufficiently large that we can compare the properties of the broad nuclear components in two different redshift bins, $z = 0.9\text{--}1.6$ and $z = 2\text{--}2.6$. Based on the results in the last sections we selected the 8, respectively 26, SFGs with $\log(M_{*}/M_{\odot}) \geq 10.9$ in these two redshift bins with firm or candidate broad emission components (implying incidences of 67 (± 24)% and 81 (± 16)%, respectively) and computed their S/N weighted co-added spectra. These are shown in the top panels of Figure 8. Qualitatively, emission line profiles with similar large [N II] $\lambda 6583/\text{H}\alpha$ ratios in their narrow and broad components and comparable broad to narrow flux ratios (upper right panel of Figure 9) are clearly detected in both redshift ranges, suggesting that the broad nuclear component phenomenon is present throughout the entire time period across the peak of the cosmic star formation epoch. However, the width of the $z \sim 1$ broad component is only 800 km s^{-1} (in the $\text{H}\alpha$ and [N II] lines), about half of that of the $z \sim 2$ co-added profile (left panel of Figure 9). It is probably premature to assign a high significance to this tantalizing difference, given the smaller sample size at the lower redshift and the intrinsic large scatter of the broad line widths of the individual detections in both redshift ranges (left panel of Figure 9). Clearly a further improvement on the statistics in the lower redshift range is highly desirable.

3.3.4. Properties of the Broad Nuclear Components as a Function of Specific Star Formation Rate

The left panel of Figure 6 shows the distribution of nuclear broad detections and candidates as a function of specific star formation rate. Within the statistical uncertainties the incidence of broad nuclear components (with or without candidates) does not seem to depend much on the vertical position in the stellar mass–star formation rate plane. The broad nuclear component profiles, broad to narrow and [N II] $\lambda 6583/\text{H}\alpha$ flux ratios above and below the main sequence also are qualitatively similar (bottom panels of Figures 8 and 9). In our decomposition of Figure 8, the average width of the broad component below the main sequence is twice as large as that above the main sequence. As with the similar difference between the average $z = 1$ and $z = 2$ profiles, this difference is tantalizing but it is not clear how much significance one should attach to it, given the large scatter in the individual line widths and the more modest sample size above the main sequence than below the main sequence.

Most surprisingly perhaps, we detect broad nuclear components just as likely significantly below the main sequence as we do near the main sequence, at least for those SFGs in which $\text{H}\alpha$ is detected at all. The average width of the broad component in the co-added spectrum of the four SFGs (with firm and candidate detections) that lie much below the main sequence is as

large as that for galaxies near the main sequence (bottom right panel of Figure 8).

The fact that the properties of the broad component depend little on specific star formation rate is highly interesting and informative in terms of the underlying physics. Tacconi et al. (2013), Magdis et al. (2012), and Saintonge et al. (2012) have presented evidence from molecular and dust observations that near the main-sequence sSFR correlates most strongly with galaxy baryonic gas fraction and star formation efficiency (the inverse of the gas depletion timescale). This suggests that the presence of the broad nuclear emission component is not strongly correlated with the gas properties on a galaxy-wide scale. The fact that the broad nuclear emission component is also not more prominent for the few outlier SFGs in our sample (at $\text{sSFR}/\text{sSFR}(\text{ms}, z) > 4$), including the very compact and high $\text{H}\alpha$ surface brightness source SA12-6339, suggests that the nuclear broad line emission is also not primarily related to compact nuclear starbursts (see also Section 4.3). Finally the detection of a broad component in galaxies one-to-two orders of magnitude below the main sequence, in one of them with AO-assisted data (SDSS1030–2026), is very exciting indeed, as this shows that the same mechanism is likely operational in red-sequence galaxies.

4. DISCUSSION

4.1. Mass Outflow Rates

In the following, we estimate the mass outflow rates as well as the momentum and kinetic energy transported in these (circum-)nuclear outflows. We assume that the nuclear broad emission represents an outflow into a cone of solid angle Ω , with a radially constant mass loss rate \dot{M}_{out} and outflow velocity v_{out} . These assumptions are motivated by recent observations of the dependence of Mg II absorber occurrence and profiles as a function of inclination of the host galaxy (Bordoloi et al. 2011; Kacprzak et al. 2011, 2012; Bouché et al. 2012), as well as theoretical work on both energy and momentum driven outflows (Veilleux et al. 2005; Murray et al. 2005; Hopkins et al. 2012). Following Veilleux et al. (2005) and Rupke et al. (2005) we take the wind outflow velocity to be the blueshifted velocity at the HWHM of the broad profile, $v_{\text{out}} \sim |\langle v \rangle_{\text{broad}} - 0.5 \times \Delta v_{\text{broad}}(\text{FWHM})|$, which is a fairly conservative estimate of the intrinsic outflow velocity (see discussion in Genzel et al. 2011). We assume that the gas is photoionized, and in case B, recombination with an electron temperature of $T_e = 10^4 \text{ K}$ (Osterbrock 1989). In our simple model (see Genzel et al. 2011) the *average* electron density and *volume filling* factor of the outflowing ionized gas scale with radius as R^{-2} (for a constant mass outflow rate) but the *local* electron density of filaments or compact clouds from which the $\text{H}\alpha$ emission originates does not vary significantly with radius and takes on a value of $\langle n_e^2 \rangle^{1/2} \sim 80 \text{ cm}^{-3}$. This choice is motivated by the average value of electron densities in the star-forming ionized gas in the disks and centers of the SFGs of our sample, as derived from the [S II] $\lambda 6716/\lambda 6731$ ratio ($\langle F(6716)/F(6731) \rangle = 1.2 \pm 0.06$), combined with the assumption that the ionized gas in the outflows is in pressure equilibrium with that star-forming gas as a result of shock excitation (Section 3.2.2). Any departure from this assumption most plausibly drives electron densities in the outflows toward lower values, in which case the values for outflow rates and mass-loading factor estimated below are lower limits.

For purely photoionized gas of electron temperature $T_4 = T_e/10^4 \text{ K}$ and case B recombination, the effective volume

emissivity is $\gamma_{\text{H}\alpha}(T) = 3.56 \times 10^{-25} T_4^{-0.91} \text{ erg cm}^{-3} \text{ s}^{-1}$, (Osterbrock 1989). The total ionized gas mass outflow rate, independent of Ω , can then be obtained from the extinction corrected, optically thin H α luminosity $L_{\text{H}\alpha,0}$ via

$$\begin{aligned} L_{\text{H}\alpha,0} &= \gamma_{\text{H}\alpha}(T) \int \Omega R^2 n_e(R) n_p(R) dR, \\ M_{\text{HII,He}} &= \mu \cdot \int \Omega R^2 n_p dR = \frac{\mu L_{\text{H}\alpha,0}}{\gamma_{\text{H}\alpha}(T) \times n_e}, \quad \text{and} \\ \dot{M}_{\text{out}} &= \Omega R^2 \mu n_p(R) v_{\text{out}} = M_{\text{HII,He}} \cdot \frac{v_{\text{out}}}{R_{\text{out}}}. \end{aligned} \quad (1)$$

Here, n_p is the proton density, $\mu = 1.36 \cdot m_p$ is the effective mass, for a 10% helium fraction, and $M_{\text{HII,He}}$ is the mass in ionized H and in He. R_{out} is the outer radius of the outflow that initially is launched near the nucleus. We take R_{out} as the half-width at half maximum radius of the broad component emission, with $\langle R_{\text{HWHM}} \rangle \sim 1.25$ kpc from an average of the spatially resolved data in FS14a and E. Wuyts et al. (2014b, in preparation).

To compute the intrinsic H α luminosity for the broad component we corrected the observed fluxes for extinction using the visual extinction toward the bulk of stellar light $A_{V,\text{stars}}$ from the best-fit SED models to the galaxies' SEDs (Section 2.1) and accounting for extra attenuation toward the nebular gas following the recipe $A_{V,\text{gas}} = A_{V,\text{stars}} \times (1.9 - 0.15 \times A_{V,\text{stars}})$ found by Wuyts et al. (2013) as a best fit for the spatially resolved rest-UV to optical SEDs and H α data of $z = 0.5$ – 1.5 SFGs from the 3D-*HST* survey (see also Price et al. 2014). As for the SED modeling, the Calzetti et al. (2000) law was assumed to calculate the continuum extinction at the wavelength of H α . This provides almost certainly a conservative lower limit to the intrinsic luminosity since the 80–140 km s $^{-1}$ blueshift of the broad line profile (relative to the narrow H α emission) in several SFGs suggests a significant amount of differential extinction within the outflowing component (see Genzel et al. 2011). The intrinsic H α luminosity from the narrow component emission was computed in the same manner and used to derive the SFRs in the nuclear regions via the Kennicutt (1998) conversion adjusted to our adopted Chabrier (2003) IMF.

Table 4 summarizes the inferred mass outflow rates, the mass-loading factors referred to the SFR in the nuclear regions, the ratios of outflow momentum rates to radiation momentum rates L/c , and the ratios of outflow kinetic energies to the luminosities of the (circum-)nuclear regions, for all 20 $\log M_* > 10.8$ SFGs with a good parameter definition of a nuclear broad component (excluding the three BLR sources). Figure 10 shows the resulting distributions of the inferred mass outflow rates and mass-loading factors in histogram form.

Keeping in mind the large uncertainties of all the numbers, resulting in systematic uncertainties of the outflow, momentum and energy rates by at least a factor of two up and down, the median mass-loading factors of the ionized outflows relative to the nuclear star formation rates are plausibly near/above unity, and the median outflow rates are about $100 M_\odot \text{ yr}^{-1}$, comparable to the values of stellar feedback driven winds in the disks of these high- z galaxies (Erb et al. 2006; Genzel et al. 2011; Newman et al. 2012). Any additional contribution from very hot ionized plasma as well as cold atomic and molecular material in the outflows would increase this estimate.

The main physical difference between the nuclear-AGN and the disk-stellar feedback cases are the large outflow velocities (see left panel of Figure 9), not the mass-loading and outflow rates (top right panel of Figure 9). The median outflow velocity

of the nuclear outflows is $\sim 500 \text{ km s}^{-1}$, more than twice that of the stellar feedback driven winds as estimated from the broad component in the outer disks and at lower masses ($v_{\text{out}}(\text{disk}) \sim 200 \text{ km s}^{-1}$). In six cases, the nuclear outflow velocity exceeds 700 km s^{-1} . Higher outflow velocities for AGN feedback is also characteristic for gas-rich, luminous AGN-ULIRGs at low- z (Sturm et al. 2011; Veilleux et al. 2013; Rupke & Veilleux 2013; Spoon et al. 2013). This means that in about half of the nuclear outflow galaxies in Table 4 the outflow velocity is at least twice the rotation velocity of the galaxy, implying that the nuclear outflows in principle can fully escape the galaxies, and perhaps even their halos. That is obviously not the case for the disk outflows. The stellar feedback likely only drives fountains where the gas will return after about a billion years or less, as indicated by recent theoretical work (Davé et al. 2011; Zhang & Thompson 2012; Übler et al. 2014).

The median ratio of the momentum in the outflows to that in (stellar) radiation is ~ 5 , and there are nine SFGs where this value is 10 or more. Such large values probably argue against momentum driven outflows (Dekel & Krumholz 2013; Krumholz & Thompson 2013). The median energy in the outflows is $\sim 0.4\%$ of the nuclear star formation luminosities. Theoretical estimates suggest that energy driven outflows can account for up to 1% of the energy source (Murray et al. 2005). Taking the nuclear star formation luminosities estimated from the narrow H α emission as a guide, radiation energy driven outflow would be possible for one half but not the other half of the sample in Table 4.

For those of our SFGs with AGN identifications (see Section 4.2), we have used the absorption-corrected X-ray luminosity, and/or the mid-IR luminosity, or a combination of both, to estimate the bolometric AGN luminosity, using the techniques of Rosario et al. (2012, for X-rays) and Richards et al. (2006, for mid-IR). Despite inhomogeneous data, it is natural to assume that these identified AGNs preferentially sample larger AGN luminosities among our targets. We list these luminosities in the next to last column of Table 1. If we only had a mid-IR estimate we assumed that this constitutes effectively an upper limit to the AGN luminosity because of contributions to the mid-IR luminosity by dusty star formation. The last column of Table 1 gives the ratio of the galaxy integrated luminosity from star formation to this AGN luminosity estimate. That ratio varies over more than an order of magnitude from source to source but on average has a value of 1.3. Since the nuclear star formation rates typically are 30%–40% of the galaxy integrated star formation rates, the mass-loading factors, as well as momentum and energy ratios in Table 4 would decrease by a factor of \sim two when compared to the AGN luminosity rather than to the nuclear stellar luminosity. This may increase the probability that the nuclear outflows are momentum driven if the AGN is active, although this conclusion carries substantial uncertainty.

Mechanical driving of the nuclear outflows may be an additional possibility, as in other low-luminosity AGNs and black hole systems (Fabian 2012; McNamara & Nulsen 2007).

Massive high- z SFGs near the main sequence are gas rich, with typically $> 10^{10} M_\odot$ of molecular gas in the central few kiloparsecs (Tacconi et al. 2013). Our observations imply that these circum-nuclear gas reservoirs can in principle be driven out by the nuclear outflows over a timescale of a few hundred megayears. If there is efficient radial transport of gas from the outer disk to the center, as advocated by many theoretical studies (Noguchi 1999; Immeli et al. 2004a, 2004b; Genzel et al. 2008; Bournaud et al. 2009; Ceverino et al. 2010; Dekel & Burkert

Table 4
Outflow Parameters

Source	Z	$\log(M_*/M_\odot)$	sSFR/sSFR (ms)	SFR (Nucleus) ($M_\odot \text{ yr}^{-1}$)	R_{HWHM} (kpc)	$F_{\text{broad}}/$ $F_{\text{narrow}} \text{H}\alpha$	$L(\text{H}\alpha)_{\text{broad,0}}$ (erg s^{-1})	v_{out} (km s^{-1})	$n(\text{e})_{\text{broad}}$ (cm^{-3})	M_{broad} (H II+He) (M_\odot)	dM/dt_{out} ($M_\odot \text{ yr}^{-1}$)	$\eta = dM_{\text{out}}/dt/\text{SFR}$ Ionized Gas	Momentum Ratio Outflow/Radiation	Energy Ratio $dE/dt/L$
	1	2	3	4	5	6	7	8	9	10	11	12	13	14
Q1623-BX663	2.43	10.81	0.664	30	1.3	1.1	6.9E+42	1300	80	2.8E+08	288	3.1	62	1.3E-01
U3-25105	2.29	10.85	0.826	32	1.3	0.7	4.6E+42	214	80	1.9E+08	32	0.3	1	3.8E-04
ZC-400528	2.39	11.04	1.768	120	1.3	0.79	2E+43	802	80	8.1E+08	513	1.7	17	2.3E-02
D3a-6397	1.50	11.08	5.052	73	1.3	0.6	9.2E+42	520	80	3.7E+08	153	0.3	5	4.7E-03
ZC-400569 central disk	2.24	11.08	1.213	92.0	1.3	0.3	5.80E+42	350	80	2.35E+08	65	0.3	1	7.2E-04
GS3_19791 (K20-ID5)	2.22	11.31	1.649	148	1.3	3.3	1.0E+44	530	80	4.2+09	1743	5.3	31	2.7E-02
D3a-6004	2.39	11.50	1.446	44	1.3	2.9	2.7E+43	420	80	1.1E+09	365	1	17	1.2E-02
J0901+1814	2.26	11.49	2.489	200	1.3	1.1	4.63E+43	323	80	1.9E+09	481	0.8	4	2.1E-03
COS4-13174	2.10	11.03	1.469	90	1.3	0.6	1.1E+43	350	80	4.6E+08	127	0.6	2	1.4E-03
COS4-6963	2.30	10.96	0.059	6.3	1.3	3	4E+42	480	80	1.6E+08	61	6.8	23	1.8E-02
GS3-22005	0.95	10.93	0.410	2.1	1.3	0.8	3.6E+41	700	80	1.5E+07	8	0.6	13	1.5E-02
U3-12280	1.03	10.98	0.516	5.7	1.3	1	1.2E+42	350	80	4.8E+07	13	0.6	4	2.4E-03
Q2343-BX610	2.21	11.00	0.548	13	1.3	0.2	5.6E+41	500	80	2.3E+07	9	0.1	2	1.4E-03
D3a-15504	2.38	11.04	0.949	24	1.3	0.7	3.5E+42	475	80	1.4E+08	54	0.3	5	4.2E-03
COS3-644	0.88	11.17	0.484	6.6	1.3	1	1.4E+42	300	80	5.6E+07	13	0.6	3	1.5E-03
U3-23710	2.53	11.03	0.309	18	1.3	1.5	5.8E+42	1300	80	2.4E+08	243	4.5	85	1.8E-01
GS3-28008	2.29	11.36	0.493	108	1.3	1	2.3E+43	300	80	9.2E+08	219	2.0	3	1.5E-03
1030-2026	2.51	11.25	0.033	7.1	1.3	10	1.5E+43	1300	80	6.0E+08	620	87.8	564	1.2E+00
COS43206	2.10	11.40	0.525	44	1.3	1.3	1.2E+43	300	80	4.9E+08	116	1.1	4	2.0E-03
COS4-11363	2.10	11.28	0.447	42	1.3	2	1.7E+43	1240	80	7.1E+08	695	8.4	103	2.1E-01

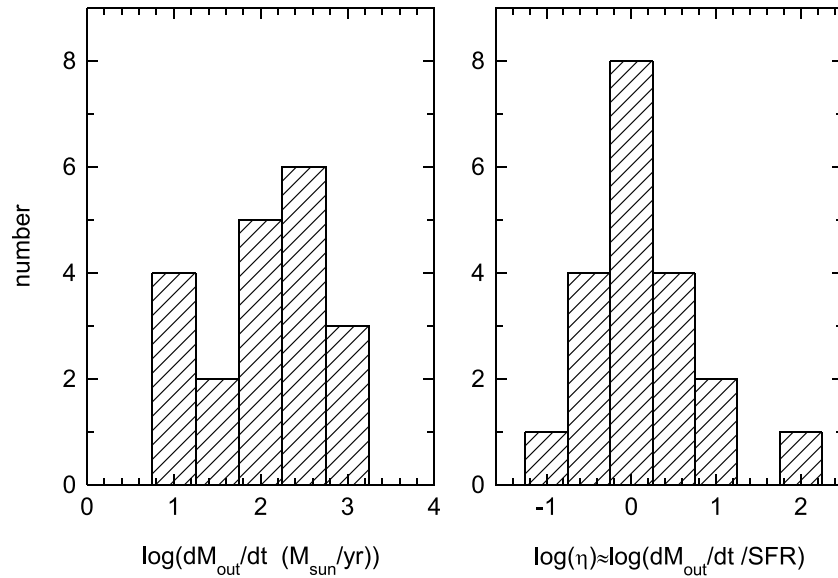


Figure 10. Inferred distribution of mass outflow rates (left) and nuclear mass-loading factors (ratio of outflow rate to star formation rate, right) inferred from the data in the 20 $\log M_* > 10.8$ SFGs with good individual broad detections (excluding those SFGs with broad line regions). See Section 4.1 and Table 4 for details.

2014; Forbes et al. 2014), the nuclear outflows may even be an efficient process for removing gas from the entire galaxy.

4.2. Correlation with X-Ray/Optical/Infrared/Radio AGNs

4.2.1. Identification of AGNs

In this section, we analyze the relationship and relative incidence of the nuclear broad emission SFGs discussed in the last section, to the AGN populations in the same cosmological fields.

For this purpose, we searched for signatures of contemporaneous nuclear activity in our sample of massive galaxies using five different tracers. X-ray imaging and catalogs are available for 91 of the 110 galaxies in Table 1 from the *Chandra* Deep Fields North/South (Alexander et al. 2003; Xue et al. 2011; Brightman & Ueda 2012), Extended *Chandra* Deep Field South (Lehmer et al. 2005), *AEGIS-X* survey (Laird et al. 2009), *Subaru XMM* Deep Field (Ueda et al. 2008) and the SDSS J1030+0524 QSO field (Farrah et al. 2004). These fields vary considerably in instrumental coverage and depth, from 4 Ms with *Chandra* in the CDF-S to 86 ks with *XMM-Newton* in the SDSS1030 pointing, spanning sensitivities going down to X-ray emitting star-forming galaxies in the deepest data to fairly luminous AGNs with X-ray luminosities of $>10^{44}$ erg s^{-1} ($z \sim 2$) in the shallowest field. Nevertheless, we proceed knowing that we may be missing a proportion of active galaxies from our sample. In total, 13 of the SFGs in Table 1 are detected in the X-rays, of which 11 are confirmed AGNs based on various X-ray diagnostics as developed by Xue et al. (2011).

Spitzer imaging and public catalogs in the four IRAC bands are available for 91 galaxies, from the GOODS-S survey (Dickinson et al. 2003), SWIRE survey (Lonsdale et al. 2003), *AEGIS* survey (Barmby et al. 2008) and SCOSMOS (Sanders et al. 2007). While the depths of the IRAC data do vary between fields, the coverage is more uniform than among the X-ray data sets. We use the criteria of Donley et al. (2012), which identify AGNs based on their observed IRAC $5.8 \mu\text{m}/3.6 \mu\text{m}$ to $8.0 \mu\text{m}/4.5 \mu\text{m}$ flux ratios. This method is fairly free of contamination from starbursts at $z \sim 2$, but may miss some weak AGNs. The IRAC flux ratios of our sample SFGs are plotted in Figure 11,

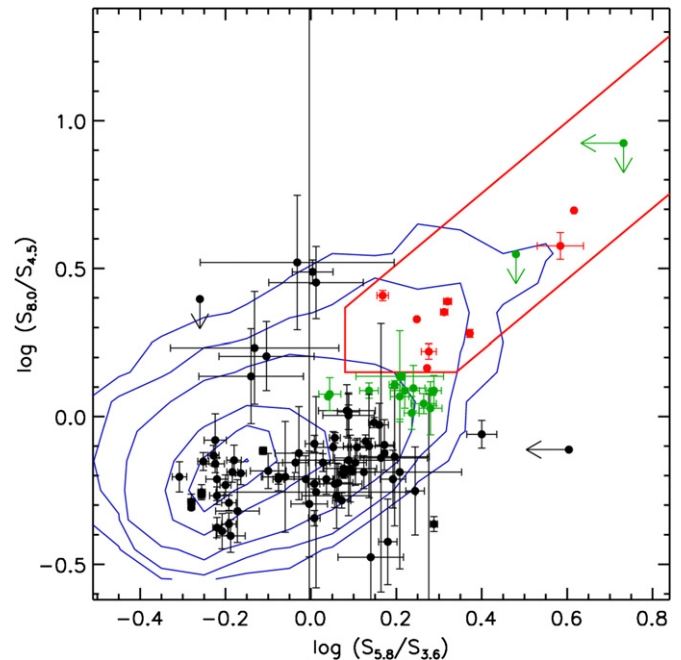


Figure 11. IRAC flux ratio plot adapted from Figure 12 of Donley et al. (2012). The blue contours in the background represent the distribution of $0.7 < z < 2.6$ galaxies based on the COSMOS IRAC catalog (SCOSMOS). Galaxies from our sample with IRAC photometry are plotted as filled black circles with error bars. The Donley et al. (2012) selection box for AGNs is shown in red and confirmed AGNs in our sample are plotted as red points. Lower-quality candidates are plotted as green points. Only a few galaxies from our sample lie within the Donley et al. (2012) region. Another small number lie close to its boundary and may contain weak AGNs.

(A color version of this figure is available in the online journal.)

along with contours indicating for reference the distribution of IRAC-detected objects from S-COSMOS in the same range of $z \sim 0.7-2.6$, and red lines enclosing the AGN selection wedge according to Donley et al. (2012). In total, nine galaxies satisfy the IRAC AGN criteria, with 15 more potential AGNs that lie close to the region delineated in Donley et al. (2012) but formally do not satisfy the criteria.

Some of the fields from which the samples are drawn have VLA 20 cm radio catalogs from VLA-COSMOS (Schinnerer et al. 2010), AEGIS-20 (Ivison et al. 2007), GOODS-N (Morrison et al. 2010), ECDF-S (Miller et al. 2013), and SXDF (Simpson et al. 2006). Of the 75 galaxies in our sample with radio coverage, 7 are detected at the depths of the corresponding surveys. Since all these fields are also covered by *Spitzer*/MIPS imaging and catalogs, we used the $24\ \mu\text{m}$ to 20 cm observed flux ratio as a way to discriminate between true radio-loud AGNs and galaxies dominated by star-formation in the radio band, following the approach of Appleton et al. (2004), but including a k -correction based on the typical star-forming galaxy SED from Wuyts et al. (2008). Only one galaxy (KMOS^{3D}-GS3-18419) is identified as radio-loud and its AGN nature is also confirmed by IRAC-based criteria.

We also used available rest-frame UV spectroscopy to search for the standard AGN emission line indicators. Four of the SFGs in Table 1 are identified as AGNs in that way (BX663, D3a15504, J0901+1814, and KMOS^{3D}-GS3-19791), as has been previously pointed out by Förster Schreiber et al. (2011, 2014a) and Fadelly et al. (2010).

In addition to the methods described above, which apply to a large fraction of the galaxies, we also searched published samples of AGNs selected by variability in the optical or X-ray in the GOODS and ECDFS fields (Trevese et al. 2008; Villforth et al. 2010; Young et al. 2012) and samples of galaxies searched for VLBI radio cores (Middelberg et al. 2011; Chi et al. 2013). Only GOODS-N-22747 was identified as an AGN in these studies, consistent with its independent identification as an X-ray AGN.

In total, we have X-ray, mid-IR, radio, or optical spectroscopy data relevant to AGN identification on 95 of the 110 SFGs in Table 1 (henceforth called the “common sample”).

4.2.2. AGN Incidence as a Function of Stellar Mass

With the AGN identifications and candidates from the last section, we find that the AGN incidence strongly varies with galaxy stellar mass, qualitatively mirroring the incidence of the broad nuclear components discussed in Section 3.3.1. Figure 12 compares the broad component with the AGN fractions in the common sample (with both AGN and broad component data) as a function of stellar mass for our SFGs, and with the fraction of AGNs among the more general population of $z \sim 1$ –2 SFGs. The green/brown and yellow/green asterisks in Figure 12 denote the AGN fractions in the common sample for the “firmly identified” AGNs and the firm plus “candidate” AGNs. The AGN fraction for $\log(M_*/M_\odot) \geq 10.9$ in the “common sample” is $38 (\pm 10)\%$. Including the AGN candidates the value would increase this value to $51 (\pm 12)\%$ (Table 3). The gray and green shaded distributions in Figure 12 denote the AGN incidence expanded to the entire GOODS N/S and COSMOS fields but corrected upward by 30% to estimate the AGN fraction in the star-forming population only. According to this estimate the AGN incidence at $\log(M_*/M_\odot) \geq 10.9$ is $28 (\pm 10)\%$. All these values are in good agreement with previous findings in the literature, although statistical uncertainties are obviously large (e.g., Kauffmann et al. 2003b; Reddy et al. 2005; Papovich et al. 2006; Daddi et al. 2007; Brusa et al. 2009; Xue et al. 2010; Hainline et al. 2012; Bongiorno et al. 2012; Rosario et al. 2013a).

At face value the incidence of broad components at $\log(M_*/M_\odot) \geq 10.9$ is about 1.5 times larger than those of the AGNs in the common sample. If the estimates of the broader COSMOS

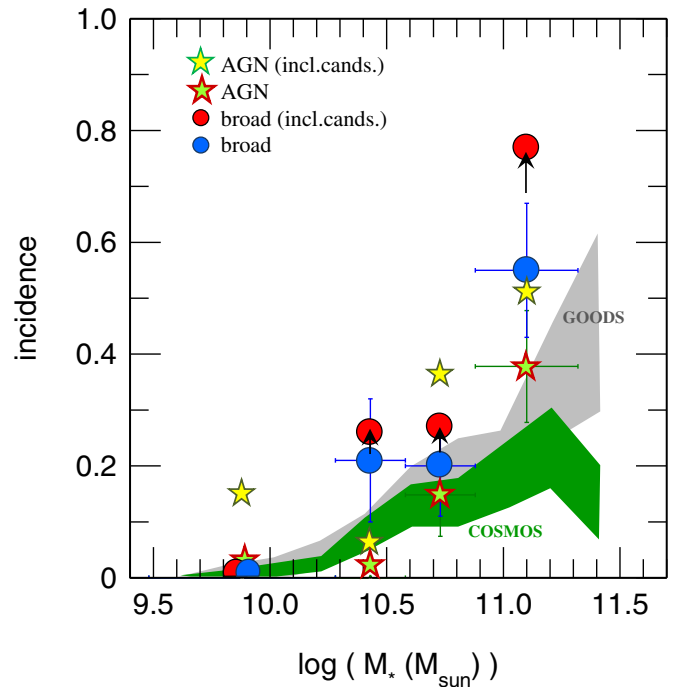


Figure 12. Comparison of the mass dependence of the incidence of broad nuclear emission and AGNs identified on the basis of X-ray/optical/infrared and radio criteria. Filled blue circles denote the incidence of firm broad nuclear component detections, and upward pointing arrows ending at the filled red circles show the incidence of the firm plus candidate broad nuclear component detections. Green/brown and yellow/green asterisks denote the incidence of firm AGNs, and AGNs including candidates in our sample (i.e., from the “common sample” described in Section 4.2.1). The gray and green shaded distributions denote the AGN incidence as a function of stellar mass as probed in the entire GOODS N/S and COSMOS fields (see Section 4.2).

(A color version of this figure is available in the online journal.)

and GOODS fields are used, that ratio increases to between 1.8 and 3.5.

Overall the data thus may suggest that the nuclear broad emission activity has approximately twice the duty cycle of AGNs in this highest stellar mass bin at/above the Schechter mass. Caution is warranted, however, to not overinterpret this potentially very interesting difference. The statistical uncertainties alone are already large enough to make up some of the difference in incidence. If one takes 0.66 as the best estimate of the broad component fraction at $\log(M_*/M_\odot) \geq 10.9$ (the average of the firm nuclear outflow sources and the number including candidates), and 0.37 as the AGN incidence (an average of the firm AGN and firm plus candidates in the common sample, and the COSMOS and GOODS numbers), the difference is statistically significant at the $\sim 2.5\sigma$ level. In addition the aforementioned variations in depth of the AGN indicators in the different fields, along with the possible effects of extinction and AGN variability would systematically increase the AGN fraction and thus further decrease the differences.

We take a conservative approach and conclude from the current evidence that the strongly mass-dependent incidence of broad nuclear components is at least as large as that of AGNs. However, if the identification of many of our candidates as broad line sources were to be confirmed, and/or statistical uncertainties further reduced, it is possible that the incidence of nuclear outflows exceeds that of luminous AGNs by a factor \sim two. Because of the more homogenous coverage and lower susceptibility to variability and extinction, the occurrence of

the broad emission may likely turn out to be a better way of characterizing the impact of massive nuclear black holes on their surroundings than the AGN light/activity.

The issue of AGN variability in particular has recently been pointed out as a major stumbling block in investigating the co-evolution of massive black holes and their host galaxies (e.g., Hickox et al. 2014). High- z AGNs of luminosity as detected in X-ray deep fields vary by few tenths of a magnitude over a few year timescale (Salvato et al. 2011; Wold et al. 2007). Studies of local AGNs suggest a power-law slope -1 in the power spectral density of light curves ($P(\nu) \propto \nu^{-\alpha}$ with $\alpha \approx 1$, e.g., McHardy et al. 2006; Webb & Malkan 2000). While it is difficult to extrapolate to very low frequency ν , large variations have been observed in the few luminous AGNs that were monitored over decades (Ulrich et al. 1997). Very large variations of the AGNs may occur over the response time of a kiloparsec-size photoionized outflow region, which will be at least thousands of years due to combined light travel and recombination timescales (where recombination time may be shorter, depending on local electron density). Observability of the outflow may be extended further into periods of unobservable direct AGN radiation if the ionizing agent is a combination of photoionization and of delayed shocks set by the AGN outbursts, as discussed in Section 3.2 (e.g., Zubovas & King 2012; Gabor & Bournaud 2014). The dynamical crossing time of the nuclear outflow regions is about 3 million years, smoothing out any variability in the nucleus and making the outflow still observable when the AGN is off or weaker. The recombination timescale in the winds and nuclear narrow line gas is probably less than the light travel time, calling for an ionization agent when AGN radiation levels are low (FS14a).

4.3. Can Nuclear Star Formation Bursts Drive the Nuclear Outflows?

We have shown in Section 3.2.2 and in Figure 5 that for a fraction of the broad nuclear outflow sources their narrow line ratios cannot be explained by stellar photo-ionization, but require an AGN or a combination of shocks, AGN, and stellar ionization. Based on the very high $[\text{N II}] \lambda 6583/\text{H}\alpha$ ratio in the stacked broad nuclear component of all $\log(M_*/M_\odot) \geq 10.9$ SFGs in the lower right panel of Figure 7, this conclusion can plausibly be extended to the average galaxy in this mass range. We have also shown that the incidence of a distinct nuclear outflow component (of much greater inferred outflow velocity than in the extended “disk” outflows) increases rapidly at or above the Schechter mass (Section 3.3). And finally, we have shown in the last Section (Section 4.2) that the incidence of AGNs as identified in X-ray/mid-IR/radio/optical spectroscopy tracers also increases rapidly at and above this mass. Taken together, these findings provide strong circumstantial evidence, but by no means a unique proof, that the broad nuclear outflows at $\log(M_*/M_\odot) \geq 10.9$ are driven by the central massive black holes.

Another constraint of the relative roles of (circum-)nuclear star formation and AGNs in accounting for the broad (circum-)nuclear outflows comes from the nuclear concentration of the narrow $\text{H}\alpha$ emission, which should track star formation. Under the counter-hypothesis that (circum-)nuclear star formation, and not AGNs, is the main driver also of the nuclear outflows (as well as the disk outflows), one would then expect that the concentration of narrow $\text{H}\alpha$ emission is more pronounced in those SFGs with well-detected central outflow components, than in the SFGs without individual detections. Enhanced extinction

in the nuclear regions would weaken such central peaks in narrow $\text{H}\alpha$ emission, but at the same time plausibly also the broad emission.

We have measured the ratio of narrow $\text{H}\alpha$ emission in the circum-nuclear region ($0''.6$ diameter for seeing limited, and $0''.35$ for AO data, as described in Section 2.2) to the galaxy integrated narrow $\text{H}\alpha$ flux for all 52 SFGs with IFU data at $\log(M_*/M_\odot) > 10.5$ for which this ratio could be reliably determined. In the remaining 11 SFGs with IFU data the narrow emission is either too faint, or the $\text{H}\alpha$ emission is totally dominated by broad emission. Of these 52 SFGs 28 have individually detected nuclear broad components (of quality 0.5, 1 or 2), 24 do not. The medians/means and standard deviations of the ratio of nuclear to total narrow $\text{H}\alpha$ flux are $0.19 (\pm 0.1)$ and $0.18 (\pm 0.09)$ for the SFGs with and without individually detected nuclear broad components, respectively. The resulting uncertainty of the mean in both groups is ± 0.02 . For comparison the flux ratio for a point source is $0.6 (\pm 0.05)$, such that the narrow $\text{H}\alpha$ emission in 50 of the 52 SFGs is significantly extended in our data. The distributions and centroids of the ratio of nuclear to total narrow $\text{H}\alpha$ flux for the two groups of SFGs are thus statistically indistinguishable, and the hypothesis that nuclear star bursts solely account for the (circum-)nuclear outflows can be rejected.

We thus conclude that the nuclear outflows are likely driven by the central massive black holes.

4.4. Stellar Mass Estimates for AGN Hosts

Given the common presence of AGNs among our sample of galaxies as discussed in the last sections, a potential concern is the reliability of the stellar masses we have been using because the emission from the AGN itself can contribute significantly or even outshine the rest-UV to near-IR emission from the stellar populations of the host galaxy. In the worst case, the inference of a mass threshold might be largely driven by the presence of a luminous AGN artificially driving up the inferred stellar masses.

From the comparison of SED fitting based on stellar population synthesis models (as used to derive the M_* and SFR estimates of our SFGs; see Section 2.1) versus a more detailed decomposition accounting for both stellar and AGN light, Santini et al. (2012) showed that stellar masses for type 2 AGNs are typically well recovered with pure stellar templates (with differences on average consistent with zero, a scatter within a factor of two, and $\sim 1\%$ of objects having larger differences). In contrast, type 1 AGNs, whose SEDs are generally more dominated by AGN light, were found to exhibit a much larger scatter of a factor of \sim six, with $\sim 30\%$ of the objects having stellar mass estimates differing by more than a factor of two, although the distribution was broadly consistent with typical differences of zero. These results are attributed to the significantly different AGN contributions to the observed SEDs between the two types. This behavior is also seen in the SEDs of our galaxies, plotted in Figure 13. Except for the three candidate BLR sources identified by their very broad line widths and their lack or weakness of forbidden line and narrow star-formation dominated emission (see Section 2.1 and Table 1), the SEDs of all galaxies including those with broad nuclear outflow signatures are consistent with being dominated by stellar emission: all show a strong Balmer/4000 Å break. The three BLR candidates show instead very blue and fairly featureless SEDs.

We conclude from this inspection that the stellar masses are very likely sufficiently reliable for most of the AGNs and broad nuclear outflow galaxies among our sample, and that possible

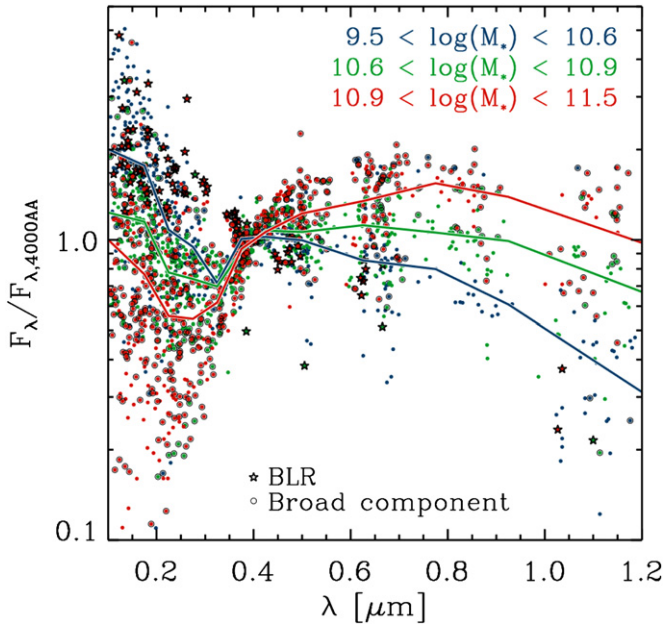


Figure 13. Rest-frame normalized spectral energy distributions of the galaxies in our sample, color-coded by their stellar mass bin as labeled in the plot. Symbols correspond to the photometry of individual galaxies, and thick lines show the median SEDs of galaxies in the three mass bins. Galaxies with a broad component are indicated with a black circle. The photometry of the three BLR sources is marked with star symbols. The BLR sources have blue SEDs, presumably due to significant contributions from nuclear emission, complicating estimates of their stellar mass content. Galaxies featuring broad outflow components on the other hand have stellar SEDs with well-pronounced Balmer 4000 Å breaks, confirming their inferred high masses.

(A color version of this figure is available in the online journal.)

associated uncertainties would not significantly affect our main findings. The stellar mass estimates for the three BLR candidates are more uncertain.

4.5. Connection to Recently Proposed Progenitor Candidates of Compact Quiescent Galaxies

Barro et al. (2013, 2014) have pointed out the presence of a population of compact $z \sim 2$ SFGs with large mass surface densities and velocity dispersions (see also Nelson et al. 2014), which may be candidate progenitors of the compact quenched galaxy population in this redshift range (e.g., van Dokkum et al. 2009; Bezanson et al. 2013; van de Sande et al. 2013; Belli et al. 2014). It is interesting to note that of the 31 $\log(M_*/M_\odot) \geq 10.9$ SFGs with firm and candidate broad nuclear components, 18 (58%) fulfill the criterion $\log(M_*/R_c^{3/2}) \geq 10.4$, and 24 (77%) fulfill a slightly more relaxed criterion $\log(M_*/R_c^{3/2}) \geq 10.0$, as proposed by Barro et al. to identify candidate progenitors of high redshift compact quiescent galaxies. The overlap between the Barro et al. high surface density SFGs and our nuclear outflow galaxies is substantial. Future work needs to explore in more detail the relation between such compact SFGs and the broad nuclear outflow phenomenon.

5. CONCLUSIONS

From high-quality seeing limited and adaptive optics observations with the SINFONI, KMOS, GNIRS, and LUCI near-infrared spectrometers, we have extracted nuclear (radius < 2.5 kpc) and outer disk $H\alpha$ /[N II]/[S II] spectra for a sample of

110 $z = 0.8$ – 2.6 “normal” star-forming galaxies with a roughly homogeneous coverage in the stellar-mass-specific star formation rate plane. Compared to our previous work (FS14a) we have increased by a factor of six the critical number of SFGs near and above the Schechter mass: 74 SFGs above $\log(M_*/M_\odot) = 10.6$ and 44 SFGs above $\log(M_*/M_\odot) = 10.9$.

We fully confirm the presence of a very common occurrence of a broad (circum-)nuclear component (FWHM ~ 450 – 5300 km s $^{-1}$) whose incidence is strongly mass dependent and not present in the outer disk spectra, in excellent agreement with FS14a. Depending on the quality cut on the individual spectra, at least half and perhaps as much as 90% of the SFGs in the mass bin $10.9 \leq \log(M_*/M_\odot) \leq 11.7$ appear to show this component, while below that threshold the occurrence drops sharply. The broad nuclear component is present above and below the main sequence of SFGs, including in several cases more than an order of magnitude below (in specific star formation rate) the main sequence, and across redshift from $z \sim 0.8$ to 2.6 , with roughly comparable width and in approximately similar strength relative to the narrow $H\alpha$ emission.

The broad component is present in $H\alpha$, [N II] and [S II]. It is spatially resolved in a subset of AO-assisted SINFONI data sets (FS14a) and one massive lensed galaxy (E. Wuyts et al. 2014b, in preparation), with a diameter of 2–3 kpc. This demonstrates that the component cannot be bound and must represent a powerful ionized nuclear wind on the scale of the classical narrow-line region of AGNs.

From the ratio of broad to narrow line fluxes in our sample, we estimate the mass loading of the warm ionized outflow component, $(dM_{\text{out}}/dt)/\text{SFR}$, to be near unity, for a local wind electron density of 80 cm $^{-3}$. If so the nuclear outflows may in principle be able to eject a significant fraction of the circum-nuclear gas out of the galaxy, and help in quenching star formation at the high mass end of the star-forming population.

For a subset of SFGs in which [N II] $\lambda 6583/H\alpha$, [S II] $\lambda \lambda 6716+6731/H\alpha$, [O I] $\lambda 6300/H\alpha$, and [O III] $\lambda 5007/H\beta$ are detected the line ratios suggest that the most likely ionization/excitation source of the nuclear outflow and nuclear narrow emission is an AGN. Alternatively a combination of shock excitation with stellar photoionization is also possible.

The $\sim 66\%$ incidence of broad nuclear emission components in the highest mass bin is at face value about twice larger than, but statistically perhaps just consistent with the incidence of AGNs in the GOODS/COSMOS fields ($\sim 30\%$), from combined X-ray, optical, infrared, and radio indicators. If this difference is real, it might be caused by AGN variability/duty cycle or extinction. Central massive black holes may drive variable or episodic outflow components that then are still observable when its radiation (the AGN) is in a low state.

Reports on outflows in AGNs at all redshifts abound in the literature. Our findings thus might at first not appear surprising. However, the key difference is that we selected galaxies on the basis of stellar mass and star formation rate, and not on the (highly variable) AGN luminosity. Our results thus imply that the majority of all galaxies at the massive tail of the population exhibit powerful outflows.

How much can the statistics be expected to improve in the next few years? Within the next year or two, we hope to increase the KMOS 3D sample at high masses by 50%, including a better coverage below the main sequence, and in the redshift range 1–1.5. Including other ongoing surveys with KMOS at the VLT and MOSFIRE at the Keck telescope, one probably can hope for an increase to about 100 galaxies in that mass range, thus

opening an excellent opportunity of mapping out the parameter dependences in more detail.

We thank the ESO Paranal staff for their excellent support with the SINFONI and KMOS observations for this work. We thank the referee for constructive and useful comments, which helped to improve the manuscript. The LBT is an international collaboration among institutions in the United States, Italy, and Germany. LBT Corporation partners are the University of Arizona on behalf of the Arizona university system; Istituto Nazionale di Astrofisica, Italy; LBT Beteiligungsgesellschaft, Germany, representing the Max-Planck Society, the Astrophysical Institute Potsdam, and Heidelberg University; The Ohio State University, and the Research Corporation, on behalf of the Universities of Notre Dame, Minnesota, and Virginia. D.J.W. and M.F. acknowledge the support of the Deutsche Forschungsgemeinschaft via Project ID 387/1–1.

REFERENCES

- Alexander, D. M., Bauer, F. E., Brandt, W. N., et al. 2003, *AJ*, **126**, 539
- Alexander, D. M., Swinbank, A. M., Smail, I., McDermid, R., & Nesvadba, N. P. H. 2010, *MNRAS*, **402**, 2211
- Allen, M. G., Groves, B. A., Dopita, M. A., Sutherland, R. S., & Kewley, L. J. 2008, *ApJS*, **178**, 20
- Appleton, P. N., Fadda, D. T., Marleau, F. R., et al. 2004, *ApJS*, **154**, 147
- Arav, N., Borguet, B., Chamberlain, C., Edmonds, D., & Danforth, C. 2013, *MNRAS*, **436**, 3286
- Arav, N., de Kool, M., Korista, K. T., et al. 2001, *ApJ*, **561**, 118
- Arav, N., Moe, M., Costantini, E., et al. 2008, *ApJ*, **681**, 954
- Arribas, S., Colina, L., Bellocchi, E., Maiolino, R., & Villar-Martin, M. 2014, *A&A*, **568**, A14
- Baldry, I. K., Glazebrook, K., & Driver, S. P. 2008, *MNRAS*, **388**, 945
- Baldwin, J. A., Phillips, M. M., & Terlevich, R. 1981, *PASP*, **93**, 5
- Barmby, P., Huang, J.-S., Ashby, M. L. N., et al. 2008, *ApJS*, **177**, 431
- Barro, G., Faber, S. M., Pérez-González, P. G., et al. 2013, *ApJ*, **765**, 104
- Barro, G., Trump, J. R., Koo, D. C., et al. 2014, *ApJ* submitted (arXiv:1405.7042)
- Behroozi, P. S., Wechsler, R. H., & Conroy, C. 2013, *ApJ*, **770**, 57
- Bell, E. F., van der Wel, A., Papovich, C., et al. 2012, *ApJ*, **753**, 167
- Belli, S., Newman, A. B., & Ellis, R. S. 2014, *ApJ*, **783**, 117
- Bezanson, R., van Dokkum, P., van de Sande, J., Franx, M., & Kriek, M. 2013, *ApJL*, **764**, L8
- Bongiorno, A., Merloni, A., Brusa, M., et al. 2012, *MNRAS*, **427**, 3103
- Bonnet, H., Abuter, R., Baker, A., et al. 2004, *Msngr*, **117**, 17
- Bonning, E. W., Shields, G. A., & Salviander, S. 2007, *ApJL*, **666**, L13
- Bordoloi, R., Lilly, S. J., Knobel, C., et al. 2011, *ApJ*, **743**, 10
- Bouché, N., Hohensee, W., Vargas, R., et al. 2012, *MNRAS*, **426**, 801
- Bournaud, F., Elmegreen, B. G., & Martig, M. 2009, *ApJL*, **707**, L1
- Bower, R. G., Benson, A. J., Malbon, R., et al. 2006, *MNRAS*, **370**, 645
- Boyle, B., Shanks, T., Croom, S. M., et al. 2000, *MNRAS*, **317**, 1014
- Brammer, G., van Dokkum, P. G., Franx, M., et al. 2012, *ApJS*, **200**, 13
- Brightman, M., & Ueda, Y. 2012, *MNRAS*, **423**, 702
- Brusa, M., Bongiorno, A., Cresci, G., et al. 2014, *MNRAS*, in press (arXiv:1409.1615)
- Brusa, M., Fiore, F., Santini, P., et al. 2009, *A&A*, **507**, 1277
- Bruzual, G., & Charlot, S. 2003, *MNRAS*, **344**, 1000
- Calzetti, D., Armus, L., Bohlin, R. C., et al. 2000, *ApJ*, **533**, 682
- Cano-Díaz, M., Maiolino, R., Marconi, A., et al. 2012, *A&A*, **537**, L8
- Cattaneo, A., Dekel, A., Devriendt, J., Guiderdoni, B., & Blaizot, J. 2006, *MNRAS*, **370**, 1651
- Cecil, G., Bland, J., & Tully, B. R. 1990, *ApJ*, **355**, 70
- Ceverino, D., Dekel, A., & Bournaud, F. 2010, *MNRAS*, **404**, 2151
- Chabrier, G. 2003, *PASP*, **115**, 763
- Cheung, E., Faber, S. M., Koo, D. C., et al. 2012, *ApJ*, **760**, 131
- Chi, S., Barthel, P. D., & Garrett, M. A. 2013, *A&A*, **550**, 68
- Conroy, C., & Wechsler, R. H. 2009, *ApJ*, **696**, 620
- Croton, D. J., Springel, V., White, S. D. M., et al. 2006, *MNRAS*, **365**, 11
- Daddi, E., Dickinson, M., Morrison, G., et al. 2007, *ApJ*, **670**, 156
- Davé, R., Oppenheimer, B. D., & Finlator, K. 2011, *MNRAS*, **415**, 11
- Davies, R. I., Agudo Berbel, A., Wieszorrek, E., et al. 2013, *A&A*, **558**, 56
- Dekel, A., & Birnboim, Y. 2006, *MNRAS*, **368**, 2
- Dekel, A., & Burkert, A. 2014, *MNRAS*, **438**, 1870
- Dekel, A., & Krumholz, M. R. 2013, *MNRAS*, **432**, 455
- Dekel, A., & Silk, J. 1986, *ApJ*, **303**, 39
- Di Matteo, T., Springel, V., & Hernquist, L. 2005, *Natur*, **433**, 604
- Dickinson, M., Giavalisco, M., & GOODS Team 2003, in *The Mass of Galaxies at Low and High Redshift: Proceedings of the European Southern Observatory and Universitäts-Sternwarte München Workshop Held in Venice, Italy, 2001 October 24–26, ESO ASTROPHYSICS SYMPOSIA*, ed. R. Bender & A. Renzini (Berlin: Springer), 324
- Diehl, H. T., Allam, S. S., Annis, J., et al. 2009, *ApJ*, **707**, 686
- Donley, J. L., Koekemoer, A. M., Brusa, M., et al. 2012, *ApJ*, **748**, 142
- Dopita, M. A., & Sutherland, R. S. 1995, *ApJ*, **455**, 468
- Efstathiou, G. 2000, *MNRAS*, **317**, 697
- Eisenhauer, F., Tecza, M., Thatte, N., et al. 2003, *Msngr*, **113**, 17
- Épinat, B., Contini, T., Le Fèvre, O., et al. 2009, *A&A*, **504**, 789
- Épinat, B., Tasca, L., Amram, P., et al. 2012, *A&A*, **539**, A92
- Erb, D. K., Steidel, C. C., Shapley, A. E., et al. 2006, *ApJ*, **646**, 107
- Fabian, A. C. 2012, *ARA&A*, **50**, 455
- Fadely, R., Allam, S. S., Baker, A. J., et al. 2010, *ApJ*, **723**, 729
- Fang, J. J., Faber, S. M., Koo, D. C., & Dekel, A. 2013, *ApJ*, **776**, 63
- Farrah, D., Priddey, R., Wilman, R., Haehnelt, M., & McMahon, R. 2004, *ApJL*, **611**, L13
- Feruglio, C., Maiolino, R., Piconcelli, E., et al. 2010, *A&A*, **518**, L155
- Fischer, J., Sturm, E., González-Alfonso, E., et al. 2010, *A&A*, **518**, L41
- Forbes, J. C., Krumholz, M. R., Burkert, A., & Dekel, A. 2014, *MNRAS*, **438**, 1552
- Förster Schreiber, N. M., Genzel, R., Bouché, N., et al. 2009, *ApJ*, **706**, 1364
- Förster Schreiber, N. M., Genzel, R., Newman, S. F., et al. 2014a, *ApJ*, **787**, 38
- Förster Schreiber, N. M., Shapley, A. E., Erb, D. K., et al. 2011, *ApJ*, **731**, 65
- Franx, M., van Dokkum, P. G., Förster Schreiber, N. M., et al. 2008, *ApJ*, **688**, 770
- Gabor, J. M., & Bournaud, F. 2014, *MNRAS*, **441**, 1615
- Genzel, R., Burkert, A., Bouché, N., et al. 2008, *ApJ*, **687**, 59
- Genzel, R., Förster Schreiber, N. M., Lang, P., et al. 2014, *ApJ*, **785**, 75
- Genzel, R., Newman, S. F., Jones, T., et al. 2011, *ApJ*, **733**, 101
- Genzel, R., Tacconi, L. J., Kurk, J. D., et al. 2013, *ApJ*, **773**, 68
- Guo, Q., White, S., Li, C., & Boylan-Kolchin, M. 2010, *MNRAS*, **404**, 1111
- Hainline, K. N., Shapley, A. E., Greene, J. E., et al. 2012, *ApJ*, **760**, 74
- Harrison, C. M., Alexander, D. M., Mullaney, J. R., & Swinbank, A. M. 2014, *MNRAS*, **441**, 3306
- Harrison, C. M., Alexander, D. M., Swinbank, A. M., et al. 2012, *MNRAS*, **426**, 1073
- Heckman, T. M. 2010, in *IAU Symp. 267, Co-Evolution of Central Black Holes and Galaxies*, ed. B. M. Peterson, R. S. Somerville, & T. Storchi-Bergmann (Cambridge: Cambridge Univ. Press), 3
- Heckman, T. M., & Best, P. N. 2014, *ARA&A*, **52**, 589
- Hickox, R. C., Mullaney, J. R., Alexander, D. M., et al. 2014, *ApJ*, **782**, 9
- Hopkins, P. F., Hernquist, L., Cox, T. J., et al. 2006, *ApJS*, **163**, 1
- Hopkins, P. F., Quataert, E., & Murray, N. 2012, *MNRAS*, **421**, 3522
- Immeli, A., Samland, M., Gerhard, O., & Westera, P. 2004b, *A&A*, **413**, 547
- Immeli, A., Samland, M., Westera, P., & Gerhard, O. 2004a, *ApJ*, **611**, 20
- Ivson, R. J., Chapman, S. C., Faber, S. M., et al. 2007, *ApJL*, **660**, L77
- Jones, T. A., Swinbank, A. M., Ellis, R. S., Richard, J., & Stark, D. P. 2010, *MNRAS*, **404**, 1247
- Kacprzak, G. G., Churchill, C. W., Evans, J. L., Murphy, M. T., & Steidel, C. C. 2011, *MNRAS*, **416**, 3118
- Kacprzak, G. G., Churchill, C. W., & Nielsen, N. M. 2012, *ApJL*, **760**, L7
- Kauffmann, G., Heckman, T. M., Tremonti, C., et al. 2003, *MNRAS*, **346**, 1055
- Kennicutt, R. C., Jr. 1998, *ARA&A*, **36**, 189
- Kewley, L. J., Dopita, M. A., Leitherer, C., et al. 2013, *ApJ*, **774**, 100
- Kewley, L. J., Dopita, M. A., Sutherland, R. S., Heisler, C. A., & Trevena, J. 2001, *ApJ*, **556**, 121
- Kewley, L. J., Groves, B., Kauffmann, G., & Heckman, T. 2006, *MNRAS*, **372**, 961
- Korista, K. T., Bautista, M. A., Arav, N., et al. 2008, *ApJ*, **688**, 108
- Kriek, M., van Dokkum, P. G., Franx, M., Illingworth, G. D., & Magee, D. K. 2009, *ApJL*, **705**, L71
- Kriek, M., van Dokkum, P. G., Franx, M., et al. 2007, *ApJ*, **669**, 776
- Krumholz, M. R., & Thompson, T. A. 2013, *MNRAS*, **434**, 2329
- Laird, E. S., Nandra, K., Georgakakis, A., et al. 2009, *ApJS*, **180**, 102
- Lang, P., Wuyts, S., Somerville, R. S., et al. 2014, *ApJ*, **788**, 11
- Law, D. R., Shapley, A. E., Steidel, C. C., et al. 2012, *Natur*, **487**, 338
- Law, R. D., Steidel, C. C., Erb, D. K., et al. 2009, *ApJ*, **697**, 2057
- Lehmer, B. D., Brandt, W. N., Alexander, D. M., et al. 2005, *ApJS*, **161**, 21
- Liu, X., Shapley, A. E., Coil, A. L., et al. 2008, *ApJ*, **678**, 758
- Liu, X., Shen, Y., Bian, F., Loeb, A., & Tremaine, S. 2014, *ApJ*, **789**, 140
- Lonsdale, C. J., Smith, H. E., Rowan-Robinson, M., et al. 2003, *PASP*, **115**, 897
- Madau, P., Ferguson, H. C., Dickinson, M. E., et al. 1996, *MNRAS*, **283**, 1388
- Magdis, G., Daddi, E., Béthermin, M., et al. 2012, *ApJ*, **760**, 6

- Mancini, C., Förster Schreiber, N. M., Renzini, A., et al. 2011, *ApJ*, **743**, 86
- Martini, P. 2004, in *Coevolution of Black Holes and Galaxies, from the Carnegie Observatories Centennial Symposia*, as part of the Carnegie Observatories Astrophysics Series, ed. L. C. Ho (Cambridge: Cambridge Univ. Press), 169
- McHardy, I. M., Koerding, E., Knigge, C., Uttley, P., & Fender, R. P. 2006, *Natur*, **444**, 730
- McNamara, B. R., & Nulsen, P. E. J. 2007, *ARA&A*, **45**, 117
- Middelberg, E., Deller, A., Morgan, J., et al. 2011, *A&A*, **526**, A74
- Miller, N. A., Bonzini, M., Fomalont, E. B., et al. 2013, *ApJS*, **205**, 13
- Morrison, G. E., Owen, F. N., Dickinson, M., Ivison, R. J., & Ibar, E. 2010, *ApJS*, **188**, 178
- Moster, B. P., Naab, T., & White, S. D. M. 2013, *MNRAS*, **428**, 3121
- Moster, B. P., Somerville, R. S., Maulbetsch, C., et al. 2010, *ApJ*, **710**, 903
- Mullaney, J. R., Alexander, D. M., Fine, S., et al. 2013, *MNRAS*, **433**, 622
- Mullaney, J. R., Daddi, E., Béthermin, M., et al. 2012, *ApJL*, **753**, L30
- Murray, N., Quataert, E., & Thompson, T. A. 2005, *ApJ*, **618**, 569
- Nelson, E., van Dokkum, P., Franx, M., et al. 2014, *Natur*, **513**, 394
- Nesvadba, N. P. H., Lehnert, M. D., De Breuck, C., Gilbert, A. M., & van Breugel, W. 2008, *A&A*, **491**, 407
- Nesvadba, N. P. H., Polletta, M., Lehnert, M. D., et al. 2011, *MNRAS*, **415**, 2359
- Netzer, H. 2013, *The Physics and Evolution of Active Galactic Nuclei* (Cambridge: Cambridge Univ. Press)
- Newman, S. F., Buschkamp, P., Genzel, R., et al. 2014, *ApJ*, **781**, 21
- Newman, S. F., Genzel, R., Förster Schreiber, N. M., et al. 2012, *ApJ*, **761**, 43
- Newman, S. F., Genzel, R., Förster Schreiber, N. M., et al. 2013, *ApJ*, **767**, 104
- Noguchi, M. 1999, *ApJ*, **514**, 77
- Osterbrock, D. 1989, *Astrophysics of Gaseous Nebulae and Active Galactic Nuclei* (A Series of Books in Astronomy; Millvalley, CA: Univ. Science Books)
- Papovich, C., Moustakas, L. A., Dickinson, M., et al. 2006, *ApJ*, **640**, 92
- Price, S. H., Kriek, M., Brammer, G. B., et al. 2014, *ApJ*, **788**, 86
- Reddy, N. A., Erb, D. K., Steidel, C. C., et al. 2005, *ApJ*, **633**, 748
- Rees, M. J., & Ostriker, J. P. 1977, *MNRAS*, **179**, 541
- Richards, G. T., Lacy, M., Storrie-Lombardi, L. J., et al. 2006, *ApJS*, **166**, 470
- Rich, J. A., Dopita, M. A., Kewley, L. J., & Rupke, D. S. N. 2010, *ApJ*, **721**, 505
- Rich, J. A., Kewley, L. J., & Dopita, M. A. 2011, *ApJ*, **734**, 87
- Rosario, D., Mozena, M., Wuyts, S., et al. 2013a, *ApJ*, **763**, 59
- Rosario, D. J., Santini, P., Lutz, D., et al. 2012, *A&A*, **545**, A45
- Rosario, D. J., Santini, P., Lutz, D., et al. 2013b, *ApJ*, **771**, 63
- Rupke, D. S. N., & Veilleux, S. 2013, *ApJ*, **768**, 75
- Rupke, D. S. N., Veilleux, S., & Sanders, D. B. 2005, *ApJS*, **160**, 115
- Saintonge, A., Lutz, D., Genzel, R., et al. 2013, *ApJ*, **778**, 2
- Saintonge, A., Tacconi, L. J., Fabello, S., et al. 2012, *ApJ*, **758**, 73
- Salvato, M., Ilbert, O., Hasinger, G., et al. 2011, *ApJ*, **742**, 61
- Sanders, D. B., Salvato, M., Aussel, H., et al. 2007, *ApJS*, **172**, 86
- Santini, P., Rosario, D. J., Shao, L., et al. 2012, *A&A*, **540**, A109
- Schinnerer, E., Sargent, M. T., Bondi, M., et al. 2010, *ApJS*, **188**, 384
- Shapiro, K. L., Genzel, R., Förster Schreiber, N. M., et al. 2008, *ApJ*, **682**, 231
- Shapiro, K. L., Genzel, R., Quataert, E., et al. 2009, *ApJ*, **701**, 955
- Shapley, A. E., Steidel, C. C., Erb, D. K., et al. 2005, *ApJ*, **626**, 698
- Sharp, R. G., & Bland-Hawthorn, J. 2010, *ApJ*, **711**, 818
- Sharples, R., Bender, R., Agudo-Berbel, A., et al. 2012, *Proc. SPIE*, **8446**, 0KS
- Sharples, R., Bender, R., Agudo-Berbel, A., et al. 2013, *Msngr*, **161**, 21
- Simpson, C., Martinez-Sansigre, A., Rawlings, S., et al. 2006, *MNRAS*, **372**, 741
- Skelton, R. E., Whitaker, K. E., Momcheva, I. G., et al. 2014, *ApJS*, **214**, 24
- Somerville, R., Hopkins, P. F., Cox, T. J., Robertson, B. E., & Hernquist, L. 2008, *MNRAS*, **391**, 481
- Spoon, H. W. W., Farrah, D., Leboutteiller, V., et al. 2013, *ApJ*, **775**, 127
- Steidel, C. C., Rudie, G. C., Strom, A. L., et al. 2014, *ApJ* in press (arXiv:1405.5473)
- Storey, P. J., & Zeppen, C. J. 2000, *MNRAS*, **312**, 813
- Sturm, E., González-Alfonso, E., Veilleux, S., et al. 2011, *ApJL*, **733**, L16
- Swinbank, A. M., Sobral, D., Smail, I., et al. 2012, *MNRAS*, **426**, 95
- Tacchella, S., Lang, P., Carollo, C. M., et al. 2014, *ApJ*, submitted
- Tacconi, L. J., Genzel, R., Smail, I., et al. 2008, *ApJ*, **680**, 246
- Tacconi, L. J., Neri, R., Genzel, R., et al. 2013, *ApJ*, **768**, 74
- Trevese, D., Boutsia, K., Vagnetti, F., Cappellaro, E., & Puccetti, S. 2008, *A&A*, **488**, 73
- Trump, J. R., Konidaris, N. P., Barro, G., et al. 2013, *ApJL*, **763**, L6
- Übler, H., Naab, T., Oser, L., et al. 2014, *MNRAS*, **443**, 2092
- Ueda, Y., Watson, M. G., Stewart, I. M., et al. 2008, *ApJS*, **179**, 124
- Ulrich, M.-H., Maraschi, L., & Urry, C. M. 1997, *ARA&A*, **35**, 445
- van de Sande, J., Kriek, M., Franx, M., et al. 2013, *ApJ*, **771**, 85
- van der Wel, A., Franx, M., van Dokkum, P. G., et al. 2014, *ApJ*, **788**, 28
- van Dokkum, P. G., Franx, M., Kriek, M., et al. 2008, *ApJL*, **677**, L5
- van Dokkum, P. G., Kriek, M., & Franx, M. 2009, *Natur*, **460**, 717
- Veilleux, S., Cecil, G., & Bland-Hawthorn, J. 2005, *ARA&A*, **43**, 769
- Veilleux, S., Meléndez, M., Sturm, E., et al. 2013, *ApJ*, **776**, 27
- Veilleux, S., & Osterbrock, D. E. 1987, *ApJS*, **63**, 295
- Villforth, C., Koekemoer, A. M., & Grogin, N. A. 2010, *ApJ*, **723**, 737
- Wake, D. A., van Dokkum, P. G., & Franx, M. 2012, *ApJL*, **751**, L44
- Webb, W., & Malkan, M. 2000, *ApJ*, **540**, 652
- Westmoquette, M. S., Clements, D. L., Bendo, G. J., & Khan, S. A. 2012, *MNRAS*, **424**, 416
- Whitaker, K. E., van Dokkum, P. G., Brammer, G., & Franx, M. 2012, *ApJL*, **754**, L29
- Wisnioski, E., Förster Schreiber, N. M., Wuyts, S., et al. 2014, *ApJ*, submitted (arXiv:1409.6791)
- Wold, M., Brotherton, M. S., & Shang, Z. 2007, *MNRAS*, **375**, 989
- Wuyts, E., Kurk, J. D., Förster Schreiber, N. M., et al. 2014a, *ApJL*, **789**, L40
- Wuyts, S., Förster Schreiber, N. M., Lutz, D., et al. 2011a, *ApJ*, **738**, 106
- Wuyts, S., Förster Schreiber, N. M., Nelson, E. J., et al. 2013, *ApJ*, **779**, 135
- Wuyts, S., Förster Schreiber, N. M., van der Wel, A., et al. 2011b, *ApJ*, **742**, 96
- Wuyts, S., Labbé, I., Förster Schreiber, N. M., et al. 2008, *ApJ*, **682**, 985
- Xue, Y. Q., Brandt, W. N., Luo, B., et al. 2010, *ApJ*, **720**, 368
- Xue, Y. Q., Luo, B., Brandt, W. N., et al. 2011, *ApJS*, **195**, 10
- Young, M., Brandt, W. N., Xue, Y. Q., et al. 2012, *ApJ*, **748**, 124
- Zahid, H. J., Kashino, D., Silvermann, J. D., et al. 2014, *ApJ*, **792**, 75
- Zhang, D., & Thompson, T. A. 2012, *MNRAS*, **424**, 1170
- Zubovas, K., & King, A. 2012, *ApJ*, **745**, 34